Computational Analysis of Shock-Boundary-Layer Interaction Mitigation in Rocket Nozzles Using Porous Bleed Geometry

a project presented to
The Faculty of the Department of Aerospace Engineering
San José State University

in partial fulfillment of the requirements for the degree

Master of Science in Aerospace Engineering

by

Mathias Joel Guillen

July 2026

approved by

Faculty Advisor
Dr. Periklis E. Papadopoulos



© 2026
Mathias Guillen
ALL RIGHTS RESERVED

ABSTRACT

Computational Analysis of Shock-Boundary-Layer Interaction Mitigation in Rocket Nozzles Using Porous Bleed Geometry

Mathias Joel Guillen

Shock-boundary-layer interactions (SBLI) within supersonic rocket nozzles can produce adverse pressure gradients, flow separation, shock unsteadiness, and associated performance losses. Although porous bleed is an established method for controlling shockwave-boundary-layer interactions (SWBLI) in supersonic inlet systems, its application within rocket nozzles remains largely unexplored. This study computationally investigates the feasibility of using downstream porous bleed to modify an internal oblique shock generated by an 11.1° concave compression corner in a converging-diverging rocket nozzle. Compressible Reynolds-averaged Navier-Stokes simulations were performed in ANSYS Fluent using a density-based solver and the SST $k-\omega$ turbulence model under near-vacuum operating conditions. Two-dimensional geometry permutations were evaluated by independently varying bleed hole quantity and diameter, followed by a three-dimensional quarter-sector model incorporating a circumferential porous region. Porous bleed effectiveness was quantified primarily through the post-shock to pre-shock static pressure ratio and the radial displacement distance of the shock-affected region at the nozzle outlet. Relative to the non-porous configuration, increasing bleed area consistently reduced both metrics. The 12-hole, 25 mm-diameter configuration reduced shock displacement distance by approximately 19.7% and pressure ratio by approximately 14.5%, while the 25-hole, 15 mm-diameter configuration produced the greatest pressure ratio reduction of approximately 16.7%. Three-dimensional analysis further demonstrated the inward radial propagation of the compression-generated shock and localized pressure disturbances associated with flow through neighboring bleed holes. Although the investigated porous configurations did not eliminate the internal shock structure, the results demonstrate that increased porous bleed area can measurably weaken its pressure signature and reduce its propagation across the nozzle flow field. These findings support porous bleed as a potential approach for internal shock control in high-expansion rocket nozzles and provide a basis for further optimization of bleed geometry, mass-flow extraction, and three-dimensional flow behavior.

Acknowledgements

I would like to express my sincere gratitude to my faculty advisor, Dr. Periklis E. Papadopoulos, for his guidance, encouragement, and valuable feedback throughout the development of this Master's Project.

I would also like to thank the Aerospace Engineering Department Chair, Dr. Nikos J. Mourtos, for his support with the organization and composition of this report and for his guidance in meeting the department's academic standards. I am additionally grateful to Dr. Yawo Ezunkpe for his thoughtful review and editorial feedback, which contributed to the clarity and quality of the final report.

I extend my appreciation to the faculty of the Aerospace Engineering Department, whose instruction and expertise provided the technical foundation applied throughout this project.

Finally, I am especially grateful to my family, friends, and colleagues for their patience, encouragement, and continued support throughout my graduate studies. Their support was instrumental in the completion of this project.

Table of Contents

Abstract ii
Acknowledgements iii
List of Figures vi
List of Tables viii
List of Symbols ix
1. Introduction 1
1.1 Motivation 1
1.2 Literature Review 1
1.2.1 Introduction and Scope 1
1.2.2 Fundamental Physics of Shockwave-Boundary-Layer Interaction 1
1.2.3 Shock-Induced Separation in Rocket Nozzles 4
1.2.4 Shockwave-Boundary-Layer Interaction Control Techniques and Approaches. 6
1.2.5 Porous Bleed as a Mechanism for Shock-Boundary-Layer Interaction Control 8
1.2.6 Modeling of Porous Bleed and CFD Approaches 9
1.2.7 Research Gap and Motivation 10
1.2.8 Summary and Research Position 11
1.3 Project Proposal 11
1.4 Methodology 11
2. Fluid Flow Mathematical Framework 13
2.1 Mathematical Formulation 13
2.2 Continuum Assumption and Knudsen Number 13
2.3 Governing Equations 13
2.4 Compressibility Parameters 14
2.5 Turbulence Modeling 15
2.6 Boundary-Layer Quantities 16
2.7 Shock-Wave Boundary-Layer Interaction 16
2.8 Boundary-Layer Response to Shock-Induced Compression 17
2.9 Porous Bleed Modeling 17
3. Rocket Nozzle Model Geometry and Sizing 19
3.1 Liquid-Propellant Rocket Engine Basis 19
3.2 Liquid-Propellant Rocket Engine Geometry Formulation 19
3.3 Computer-Aided Design Model Geometries 23
3.3.1 Control Rocket Nozzle Geometry Configuration 23
3.3.2 Concave Corner Rocket Nozzle Geometry Configuration 25
3.3.3 Porous Bleed Region Geometry Configurations 26
3.3.4 Three-Dimensional Model Geometry Configuration and Considerations 27
4. Numerical Computation Setup 29
4.1 Mesh Generation for Solid Model Geometries 29
4.1.1 Model Geometry Meshing for 2D Consideration 29
4.1.2 Model Geometry Meshing for 3D Consideration 31

4.2 ANSYS Fluent Simulations 32
5. Results and Discussion 34
5.1 Computational Flow Field Analysis 34
5.1.1 Control Nozzle Geometry Flow Simulation 34
5.1.2 Flow Simulation of Compression Corner without Porosity 35
5.1.3 Flow Simulation of Porous Bleed Region with Variation in Hole Quantity 36
5.1.4 Flow Simulation of Porous Bleed Region with Variation in Hole Diameter 37
5.2 Flow Simulation of Symmetric 3D Geometry 39
5.3 Numerical Results and Performance Trends 41
6. Conclusion 46
References 47
Appendix A: Control Configuration Engineering Drawing 49
Appendix B: ANSYS Fluent Residuals Charts 50
Appendix C: MATLAB Script: Outlet Data Analysis for Varying Hole Quantity Configurations 51
Appendix D: MATLAB Script: Outlet Data Analysis for Varying Hole Diameter Configurations 58
Appendix E: MATLAB Script: Wall Data Analysis for Varying Hole Quantity Configurations 65
Appendix F: MATLAB Script: Wall Data Analysis for Varying Hole Diameter Configurations 67

List of Figures

Fig. 1.1 Turbulent oblique SWBLI schematic. 2
Fig. 1.2 Flow reversal contours: high Re (a) 6.0°; low Re (b) 5.5°; (c) 8.0°; (d) 9.5°. Reference for iso-contour lines for vertical velocity shown '1' indicated the approx. mean sonic line. 3
Fig. 1.3 Sketch of the mach 2.9, 24° compression ramp flow. 4
Fig. 1.4 Flow separation structure and position sensitivity results. 5
Fig. 1.5 Shock over single resonant tone period, St_r, for varying time steps. z-averaged schlieren contours shown in grayscale, blue contours highlight negative x-velocities, orange arrows show shock propagation direction, black arrows show backflow. 6
Fig. 1.6 Wall-normal velocity standard deviation from particle image velocimetry (PIV) data and TU Delft (TUD) test case. 7
Fig. 1.7 Schlieren images of impinging SWBLI results compared to baseline 8
Fig. 1.8 Displacement thickness reduction as a function of plenum pressure ratio p_{pl}/p_t for boundary layer profiles 15mm downstream of bleed region on a plate with high Re (HR). 9

Fig. 3.1 Chamber relations from throat diameter 20
Fig. 3.2 Divergent neck, θ_n, and exit parabolic, θ_e, angles as a function of expansion area ratio. 22
Fig. 3.3 Isometric view of the 3D rocket engine control configuration model. 23
Fig. 3.4 Full view of the rocket engine control configuration design sketch in [mm]. . 24
Fig. 3.5 Zoomed view of the rocket engine control configuration design sketch in [mm]. 25
Fig. 3.6 2D symmetric solid surface of the rocket engine control configuration. 25
Fig. 3.7 Schematic of concave compression corner at 11.1° ramp angle. 26
Fig. 3.8 Solid Surface of concave compression corner at 11.1° ramp angle. 26
Fig. 3.9 Porous bleed region with varying bleed hole number configurations with identical diameters of 25 mm; a) 4 symmetric holes, b) 8 symmetric holes, c) 12 symmetric holes. 26
Fig. 3.10 Porous bleed region with varying bleed hole diameter configurations with constant 25 hole number; a) 5 mm bleed hole diameter, b) 10 mm bleed hole diameter, c) 5 mm bleed hole diameter. 27
Fig. 3.11 Axisymmetric 3D model with 1050 bleed outlets in square-grid in bleed region at one-quarter volume. 27
Fig. 3.12 Axisymmetric 3D model with porous bleed region and full-length rocket engine volume. 28

Fig. 4.1 Full view of the 2D symmetric solid surface regions of the control configuration. 29
Fig. 4.2 Full view of the 2D symmetric mesh of the control configuration. 30
Fig. 4.3 Zoomed view of the 2D symmetric mesh of the control configuration. 30

Fig. 4.4 Full view of the 2D symmetric mesh of the variable diameter 15 mm configuration. 30
Fig. 4.5 Zoomed view of the 2D symmetric mesh of the variable diameter 15 mm configuration. 31
Fig. 4.6 Three-dimensional mesh with one-quarter volume..... 32

Fig. 5.1 Pressure contour of the 2D symmetric fluent flow..... 34
Fig. 5.2 Mach contour of the 2D symmetric fluent flow..... 35
Fig. 5.3 Static pressure distribution of full 2D rocket geometry with compression corner and null porosity..... 35
Fig. 5.4 Static pressure distribution of full 2D rocket geometry with porous bleed region at a 4-hole configuration of 25 mm diameter. 37
Fig. 5.5 Static pressure distribution of full 2D rocket geometry with porous bleed region at a 8-hole configuration of 25 mm diameter. 37
Fig. 5.6 Static pressure distribution of full 2D rocket geometry with porous bleed region at a 12-hole configuration of 25 mm diameter. 37
Fig. 5.7 Static pressure distribution of full 2D rocket geometry with porous bleed region at a 25 hole configuration of 5 mm diameter..... 38
Fig. 5.8 Static pressure distribution of full 2D rocket geometry with porous bleed region at a 25 hole configuration of 10 mm diameter. 38
Fig. 5.9 Static pressure distribution of full 2D rocket geometry with porous bleed region at a 25 hole configuration of 15 mm diameter. 38
Fig. 5.10 Static pressure distribution along full-length rocket nozzle wall. 39
Fig. 5.11 Static pressure contour of porous bleed region with 25 bleed holes with a 15 mm diameter. 40
Fig. 5.12 Static pressure distribution at porous region wall with hole-gap interaction.. 41
Fig. 5.13 Static Outlet Pressure Distribution with Variable Bleed Hole Number..... 42
Fig. 5.14 Static Outlet Pressure Distribution with Variable Bleed Hole Diameter. 43
Fig. 5.15 Shock profile comparison of static pressure for the variable hole quantity geometries..... 43
Fig. 5.16 Shock profile comparison of static pressure for the variable hole diameter geometries..... 43
Fig. 5.17 Variation in bleed hole number geometry configurations; trends in pressure ratio and displacement distance. 44
Fig. 5.18 Variation in bleed hole diameter geometry configurations; trends in pressure ratio and displacement distance..... 45

Fig. A.1 Engineering drawing of 3D rocket engine control configuration in SolidWorks..... 49

Fig. B.1 Example simulation residuals result for the variable hole diameter 2D symmetric geometry. 50
Fig. B.2 Example simulation residuals result for the 3D axisymmetric quarter-volume geometry..... 50

List of Tables

Table 3.1 Merlin-1D Vacuum Specifications 19
Table 3.2 Typical Combustion Chamber Characteristic Length (L^*) for Various Propellant Combinations 21
Table 3.3 Collated Baseline Rocket Engine Characteristics 24

Table 4.1 Control Configuration Simulation Settings 33

Table 5.1 Local Average and Extrema Pressures along Porous Region Wall, p_2 36
Table 5.2 Performance Metric Results of Geometry Permutation at Nozzle Outlet 42

List of Symbols

Symbol	Definition	Units (SI)
θ_{def}	flow deflection angle	$^\circ$
β	shock angle	$^\circ$
M_n	Mach number of the n-region	—
γ	specific heat ratio of Air (≈ 1.4)	—
$W = \dot{m}$	mass flow rate	kg/s
Φ	porosity	—
A_{region}	cross-sectional area per region	m^2
p	pressure	Pa
R	specific gas constant	$J/kg^\circ K$
T	temperature	$^\circ K$
p_1	static free-stream pressure	Pa
p_2	static post-shockwave pressure	Pa
ρ	density	kg/m^3
Kn	Knudsen number	—
λ	molecular mean free path	μm
L	characteristic length scale	*varies*
u_{ijk}	velocity component in the x_{ijk}-direction	m/s
σ_{ij}	viscous stress tensor	Pa
δ_{ij}	Kronecker Delta	—
E	total energy per unit mass	J/kg
e	internal energy per unit mass	J/kg
c_v	specific heat at specific volume	$J/kg^\circ K$
q	heat flux	$J/s \cdot m^2$
k	thermal conductivity	$J/s \cdot m^\circ K$
μ	dynamic viscosity	$kg/m \cdot s$
V	velocity magnitude	m/s
a	speed of sound	m/s
Re	Reynolds Number	—
τ	shear stress tensor	Pa
δ	velocity boundary-layer thickness	m
δ^*	displacement thickness	m
θ_{MT}	displacement thickness	m
U_e	velocity at the outer edge of the boundary layer	m/s
k_t	turbulent kinetic energy	J/kg
ω	specific dissipation rate	$1/s$
C_f	skin friction coefficient	—
Subscripts		
B	boundary surface	—
i, j, k	general coordinate indices	—
θ	boundary momentum thickness	—
e	boundary-layer edge	—

t	turbulent	—
f	skin-friction	—
w	wall	—
bleed	bleed region	—
sonic	sonic or free region	—
def	deflection	—
MT	momentum thickness	—
Superscripts		
R	Reynolds	—
¯	Reynolds averaged	—
˜	Favre averaged	—
”	fluctuations relative to mean	—
Acronyms		
SBLI	Shock-Boundary-Layer Interaction	—
SWBLI	Shock-Wave Boundary-Layer Interaction	—
CFD	Computational Fluid Dynamics	—
RANS	Reynolds-Averaged Navier-Stokes	—
SA	Spalart-Allmaras	—
SST	Shear-Stress-Transport	—
DSMC	Direct Simulation Monte Carlo	—
DAC	DSMC Analysis Code	—
BLAM	Boundary-Layer Adjusted Model	—
VHS	Variable Hard Sphere	—
VSS	Variable Soft Sphere	—

1 Introduction

1.1 Motivation

In confined supersonic flows, concave, or compression, corner deflections generate oblique shocks governed by classical θ–β–M relations [1]. In practical viscous flows shock–boundary-layer interaction may induce local separation, elevated wall-pressure gradients, and unsteady structural loading. The resulting behavior can lead to undesirable performance characteristics as a result wall geometry [1].

Historically, the former interactions are linked to performance losses and side-load phenomena in rocket nozzles. While porous bleed is historically used in supersonic inlets to control shock-induced separation, its application within rocket nozzles remains largely unexplored [2]. This project aims to shed further light on the impact of porous bleed on SBLI in specifically rocket nozzles.

1.2 Literature Review

1.2.1 Introduction and Scope

Shock–boundary-layer interaction (SBLI) is one of the most significant and challenging phenomena encountered in compressible flows. It arises when a shockwave interacts with a viscous boundary layer, producing complex coupled effects that include boundary-layer thickening, flow separation, shock distortion, and unsteady flow behavior. These interactions are particularly important in internal flow systems such as supersonic inlets and rocket nozzles, where geometric confinement amplifies the coupling between inviscid and viscous processes.

The adverse effects of SBLI include increased total pressure losses, reduced flow uniformity, elevated thermal loads, and potentially severe unsteady structural forces. In propulsion systems, these consequences translate directly into performance penalties and design limitations [1]. While SBLI has been extensively studied in external aerodynamics and inlet configurations, its control within rocket nozzles remains comparatively underdeveloped.

The present work focuses on the application of porous bleed to mitigate SBLI within a supersonic rocket nozzle, where the objective is to determine whether a downstream porous region can weaken or suppress an oblique shock generated by a concave wall corner, thereby reducing or eliminating separation. This represents a novel extension of established inlet bleed concepts to a nozzle environment, particularly under vacuum-representative conditions relevant to space propulsion.

To support this investigation, the following reviews the current state of knowledge in SWBLI/SBLI physics, nozzle flow separation, flow control methodologies, porous bleed mechanisms, and computational modeling approaches.

1.2.2 Fundamental Physics of Shockwave-Boundary-Layer Interaction

The physics of SWBLI is governed by the interaction between compressible shock waves and viscous boundary layers. In an inviscid framework, oblique shocks are described by classical

relations such as the θ-β-M equation, which relates flow deflection angle, shock angle, and Mach number [1]. However, the presence of a boundary layer fundamentally alters this behavior.

$$\tan\left(\theta_{def}\right) = 2\cot(\beta)\frac{M_1^2\sin^2\beta - 1}{M_1^2(\gamma + \cos 2\beta) + 2} \tag{1.1}$$

Within a turbulent boundary layer, the velocity profile near the wall contains a significant portion of low-momentum fluid. When a shock wave imposes a rapid pressure rise, this low-momentum fluid may be unable to overcome the adverse pressure gradient, resulting in flow reversal and separation. The separated region typically forms a recirculation bubble bounded by a shear layer, which interacts with the incoming flow and the shock system.

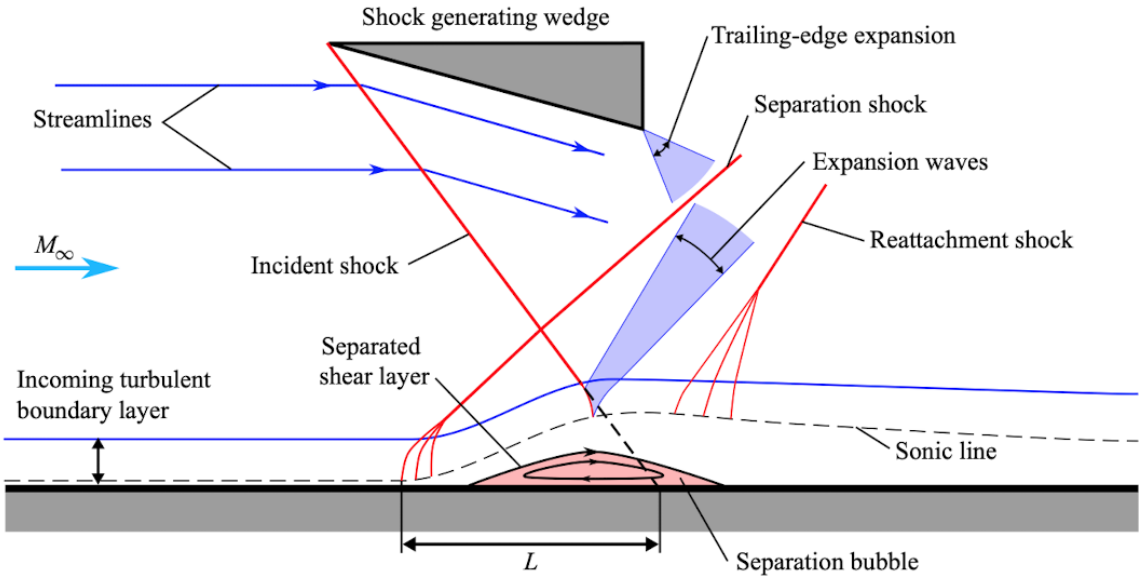


Fig. 1.1 Turbulent oblique SWBLI schematic [3].

SWBLI is commonly classified into weak and strong interaction regimes [4]. In weak interactions, the boundary layer remains attached, and the primary effect is a thickening of the velocity profile. In strong interactions, separation occurs, leading to large-scale flow restructuring [2]. Souverein et al. [5] demonstrated that the interaction strength parameter, which incorporates shock intensity and boundary-layer properties, governs the transition between these regimes. By varying the shock angle at low and high Reynolds number cases the height and strength of the induced separation bubble could be picked out, and furthermore, a distinction of when flow reversal would occur could be mapped. Their work showed that as interaction strength increases, both separation size and unsteadiness amplitude increase significantly.

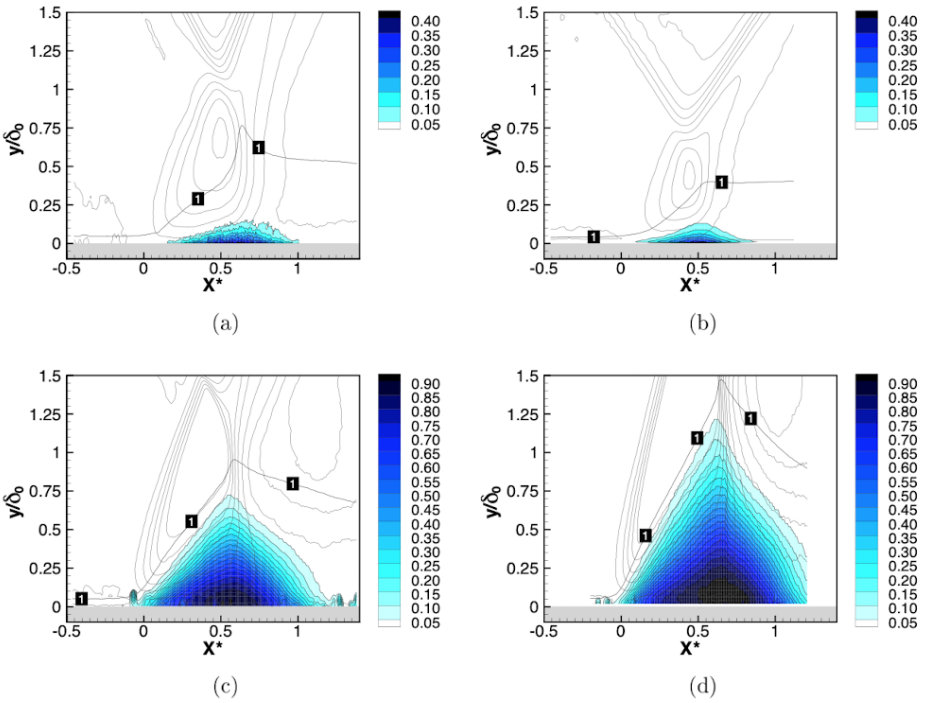


Fig. 1.2 Flow Reversal contours: high Re (a) 6.0°; low Re (b) 5.5°; (c) 8.0°; (d) 9.5°. Reference for iso-contour lines for vertical velocity shown '1' indicated the approx. mean sonic line [5].

One of the defining characteristics of separated SWBLI is low-frequency unsteadiness, reinforced by the Souverein et al. [5] study. This occurrence, often described as an oscillatory motion of the separation bubble, involves large-scale oscillations of the shock system. Zebiri et al. [6] investigated this behavior in overexpanded nozzle flows using large-eddy simulation (LES) and found that the oscillations are driven by a feedback loop between the separated shear layer and downstream pressure conditions. The study also found that shock position is strongly coupled to the effective nozzle geometry downstream of the shock by means of the system seeking pressure balance, but results in low-frequency pressure oscillations, impacting the shock position. Essentially, variations in the recirculation region alter the effective back pressure, which in turn shifts the shock location, reinforcing the unsteady feedback cycle.

From what we can see thus far, the turbulence structure within SWBLI further complicates the interaction. Smits and Dussauge [4] provided a comprehensive analysis of compressible turbulent shear layers, highlighting their role in momentum transfer and energy dissipation.

In the context of this study of internal nozzle flows, the concave corner configuration is most appropriately interpreted as a compression-corner shock–boundary-layer interaction rather than a free-standing shock. As discussed by Smits and Dussauge [4], when a supersonic boundary layer encounters a concave wall deflection, the imposed flow turning generates a compression system that interacts directly with the near-wall flow, producing a compression-corner SBLI in the absence of a second-wall impingement (seen commonly in aircraft engine implementations). The strength of this interaction is governed primarily by the corner turning angle, α (according to Smits and Dussauge [4]): weak deflections may result in distributed compression with limited boundary-layer response, whereas stronger corners produce a sharp adverse pressure gradient capable of inducing significant boundary-layer thickening, separation, and unsteady shock motion. From this, the corner-induced

shock structure and the downstream flow field cannot be treated independently; rather, they are coupled through the boundary-layer response.

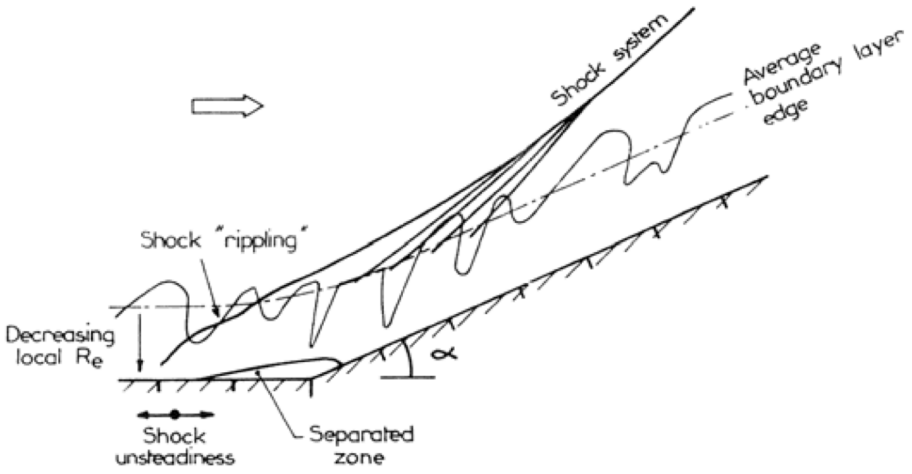


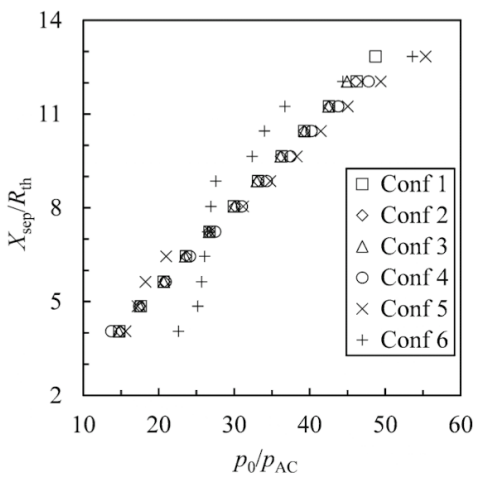
Fig. 1.3 Sketch of the mach 2.9, 24° compression ramp flow [4].

This framework provides the physical basis for considering downstream porous bleed as a control mechanism, wherein modification of the low-momentum near-wall region and pressure recovery process may, in turn, alter the global characteristics of the compression-corner interaction and its associated internal shock structure. These findings underscore the inherently multi-scale nature of SBLI, requiring simultaneous consideration of shock dynamics, turbulence modeling, and viscous transport.

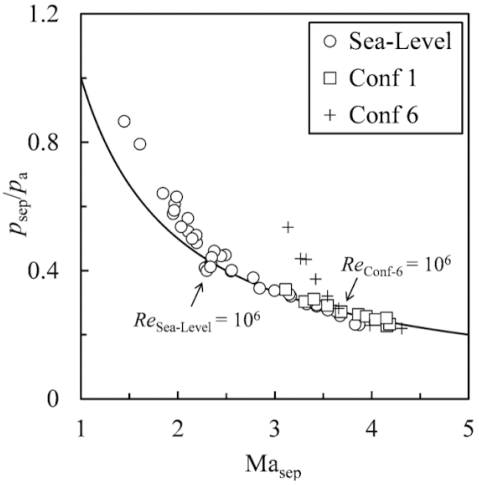
1.2.3 Shock-Induced Separation in Rocket Nozzles

It is important to consider the commonly observed shock-induced flow separation in rocket nozzles, as seen from a common case in overexpanded nozzles. In these flows, the internal pressure distribution must adjust to external ambient conditions, leading to the formation of shocks within the divergent section of the nozzle. When the wall pressure falls below ambient pressure, an internal shock forms to re-equilibrate the flow, often triggering boundary-layer separation. Overexpansion is observed in in-atmospheric conditions where the ambient back pressure is present; a common challenge in the aerospace industry today.

Stark and Génin [7] conducted experimental investigations into nozzle flow separation under varying ambient densities and demonstrated that separation location is highly sensitive to the nozzle pressure ratio (NPR), p_0/p_a and ambient density scaling, ρ_0. Their results indicate that traditional sea-level testing methods may not accurately represent high-altitude behavior, as changes in ambient density significantly alter the flow structure.



(a) Separation position as a function of nozzle pressure ratio (NPR).



(b) Separation pressures of sea-level vs. altitude chamber.

Fig. 1.4 Flow separation structure and position sensitivity results [7].

The consequences of nozzle separation extend beyond local flow disruption. Hu et al. [8] showed that separation leads to asymmetric pressure distributions and aeroelastic coupling within the nozzle structure. Their work identified two primary separation modes: free shock separation (FSS), where the separated flow remains detached from the wall, and restricted shock separation (RSS), where reattachment occurs downstream. Both modes are associated with significant unsteadiness and can produce large side-loads that impose severe structural constraints.

Numerical studies have further clarified the mechanisms underlying these phenomena. Zebiri et al. [6] demonstrated that the unsteady motion of separation-induced shocks is influenced by large-scale turbulent structures and downstream flow conditions. Their findings suggest that modifications to the boundary layer upstream or within the interaction region could alter the overall shock system and potentially reduce the unsteadiness effectiveness.

Despite substantial progress in characterizing overexpanded nozzle flows, most studies have focused on global separation driven by shock-induced re-compression of the induced flow. In contrast, under-expanded nozzle operation is typically dominated by expansion processes and does not inherently produce the same large-scale internal shock-induced separation compared to that of overexpanded nozzles. However, localized geometric features within the nozzle, such as small concave wall deflections, or contour imperfections such as compression corners, can introduce embedded compression regions that generate oblique shock structures and impose adverse pressure gradients on the near-wall flow. These localized interactions can produce compression corner type SWBLI behavior within an otherwise expansion dominated environment, thereby influencing the internal shock structure and boundary-layer state in a more subtle but still coupled manner.

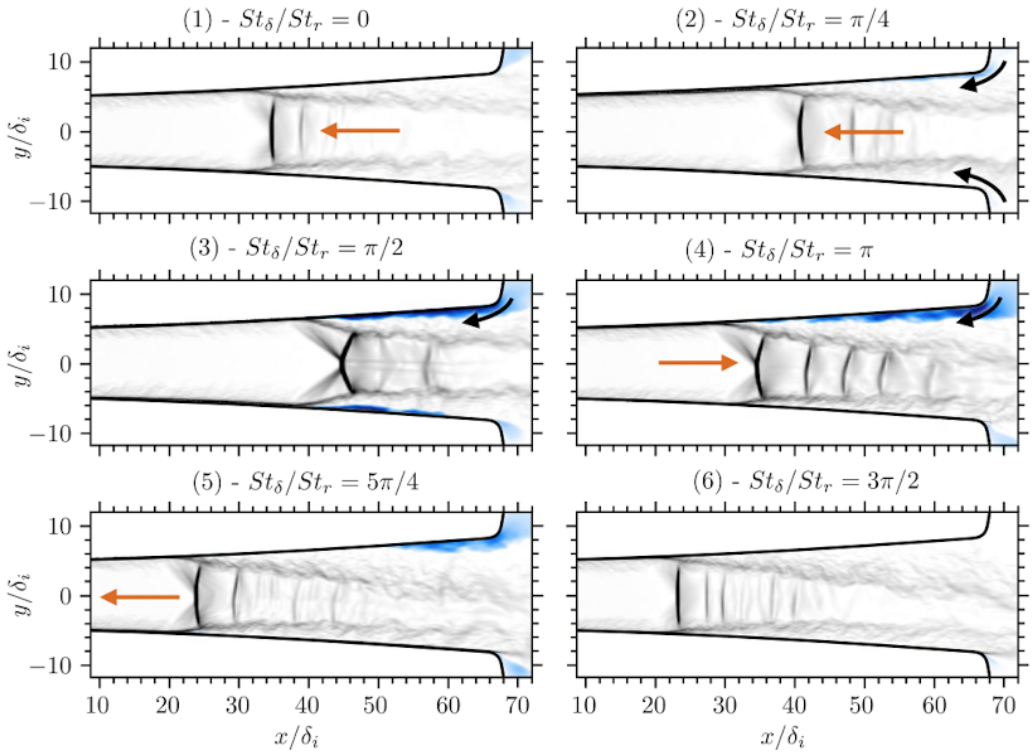


Fig. 1.5 Shock over single resonant tone period, St_r, for varying time steps. z-averaged schlieren contours shown in grayscale, blue contours highlight negative x-velocities, orange arrows show shock propagation direction, black arrows show backflow [6].

This distinction motivates a shift in focus from global separation behavior to localized control of internal shock structures in under-expanded nozzles. In particular, modifying the downstream boundary-layer properties, such as through porous bleed, offers a potential pathway to influence these embedded interactions indirectly by altering the pressure recovery and momentum distribution near the wall. As such, the present study extends traditional SBLI concepts, developed primarily for overexpanded conditions, to examine how controlled boundary-layer modification may affect internal shock formation and stability in under-expanded nozzle flows.

1.2.4 Shockwave-Boundary-Layer Interaction Control Techniques and Approaches

A range of strategies has been explored to mitigate SWBLI effects, with the primary objective of reducing separation and unsteadiness. These strategies can be categorized as passive or active control methods, depending on whether they rely on fixed geometric modifications or require external energy input.

Passive methods rely on geometric modifications to redistribute the pressure field and modify the boundary-layer response. One prominent example is the use of shock control bumps, which are designed to replace a single strong compression with a sequence of weaker compression waves. Missing et al. [3] demonstrated that bumps shaped to match the time-averaged separation bubble can greatly reduce separation in oblique SWBLI. Their work showed that the bump geometry introduces staged and progressive pressure rises that remain below the separation threshold, while an expansion fan near the bump crest locally offsets the shock-induced pressure increase. This combined effect

reduces both the extent of separation and the associated low-frequency unsteadiness by preventing the formation of a large, coherent separation bubble.

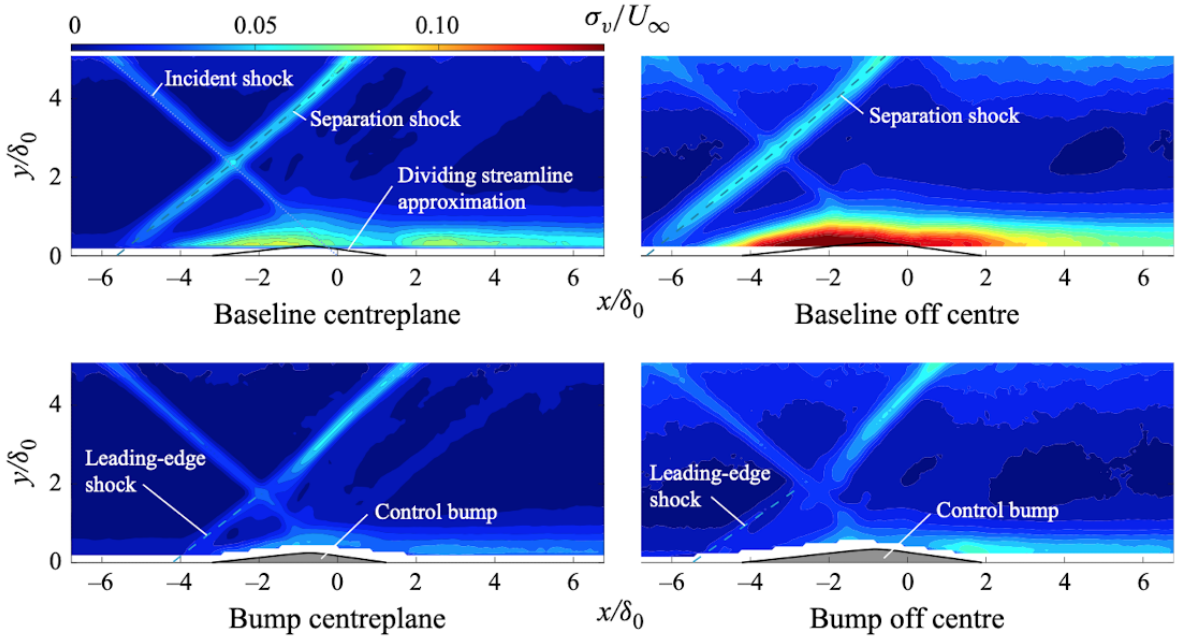


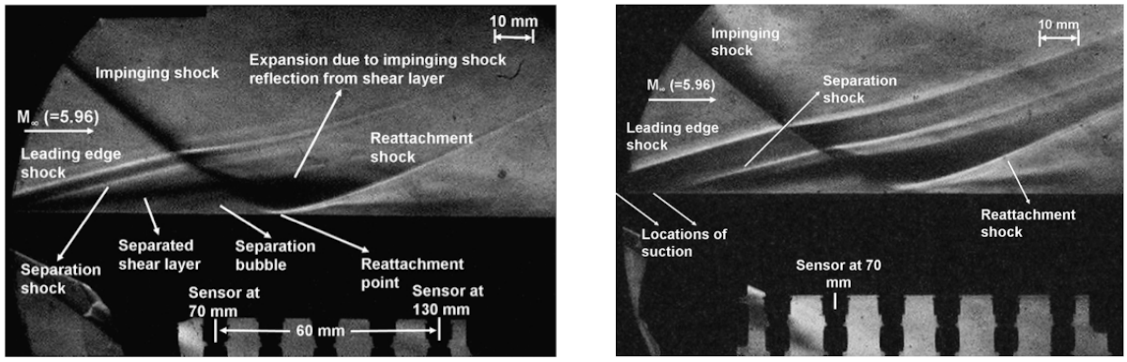
Fig. 1.6 Wall-normal velocity standard deviation from particle image velocimetry (PIV) data and TU Delft (TUD) test case [3].

Another widely studied passive technique is the use of vortex generators, which act by introducing streamwise vortices that transport high-momentum fluid from the outer flow toward the wall. As described by Sriram and Jagadeesh [2], this momentum exchange strengthens the near-wall flow and increases the boundary layer's resistance to adverse pressure gradients introduced by shocks. While such devices are effective in reducing separation length and improving flow attachment, they generally do not eliminate separation entirely and may incur drag penalties due to additional surface perturbations.

Active control methods provide greater flexibility and manipulation by directly modifying the flow through external energy implementation. These include fluid injection, suction, and plasma-based actuation. Giehler et al. [9] highlight that fluidic approaches, such as air-jet vortex generators, can replicate the effects of mechanical vortex generators while offering tunability across operating conditions and mitigates resulting drag penalties. Similarly, applying Joule heat methods such as plasma actuators introduce localized energy addition that alters the boundary-layer structure and can delay or mitigate separation. Although these methods allow for adaptive control, they introduce added system complexity and energy requirements, which can limit their practical implementation in propulsion systems.

Among all available techniques, boundary-layer suction (implemented as porous bleed) has emerged as one of the most physically direct and widely adopted control strategies, particularly in internal flows. Both Sriram and Jagadeesh [2] and Giehler et al. [9] emphasize that porous bleed operates by removing low-momentum fluid from the near-wall region, thereby thinning and "energizing" the boundary layer. This modification increases the boundary layer's ability to

withstand the imposed adverse pressure gradient, leading to reductions in separation extent and, in some cases, partial or complete suppression of separation bubbles in shock systems. Importantly, these studies also note that the effectiveness of bleed is highly sensitive to its placement relative to the interaction region and to geometric parameters such as hole size, spacing, and porosity.



(a) Schlieren image of baseline impinging SWBLI.

(b) Schlieren image of impinging SWBLI in presence of suction.

Fig. 1.7 Schlieren images of impinging SWBLI results compared to baseline [2].

These approaches demonstrate that effective SWBLI control fundamentally relies on modifying and tuning the balance between imposed pressure gradients and boundary-layer momentum regimes. Passive methods redistribute the pressure field, while active methods and bleed directly alter the boundary-layer. This distinction is particularly relevant for internal flows, where control strategies that target the near wall region (i.e. porous bleed), offer a promising pathway for influencing not only separation behavior but also the overall shock structure.

1.2.5 Porous Bleed as a Mechanism for Shock-Boundary-Layer Interaction Control

Porous bleed functions by removing low-momentum fluid from the near-wall region, thereby strengthening the boundary layer and increasing its resistance to separation. This process reduces the effective displacement thickness and alters the velocity profile, allowing the boundary layer to better withstand the adverse pressure gradient imposed by a shock.

Experimental evidence for the effectiveness of bleed is well established. Sriram and Jagadeesh [2] conducted shock tunnel experiments at hypersonic conditions and demonstrated that both suction and tangential blowing can significantly reduce separation length. Their results showed reductions of up to 13.33% for suction and 20% jet injection, even when the bleed mass flow rate was an order of magnitude smaller than the boundary-layer mass defect for the jet injection scenario.

More recent work by Giehler et al. [9] provided a comprehensive investigation of porous bleed systems across both supersonic and subsonic regimes. Their study combined experimental measurements with Reynolds-averaged Navier–Stokes (RANS) simulations and showed strong agreement between the two. Importantly, they identified significant three-dimensional effects, including spanwise variations in boundary-layer profiles and interactions with corner flows. These findings indicate that bleed performance has an inherent nuance regarding its observed behavior in two and three dimensional models.

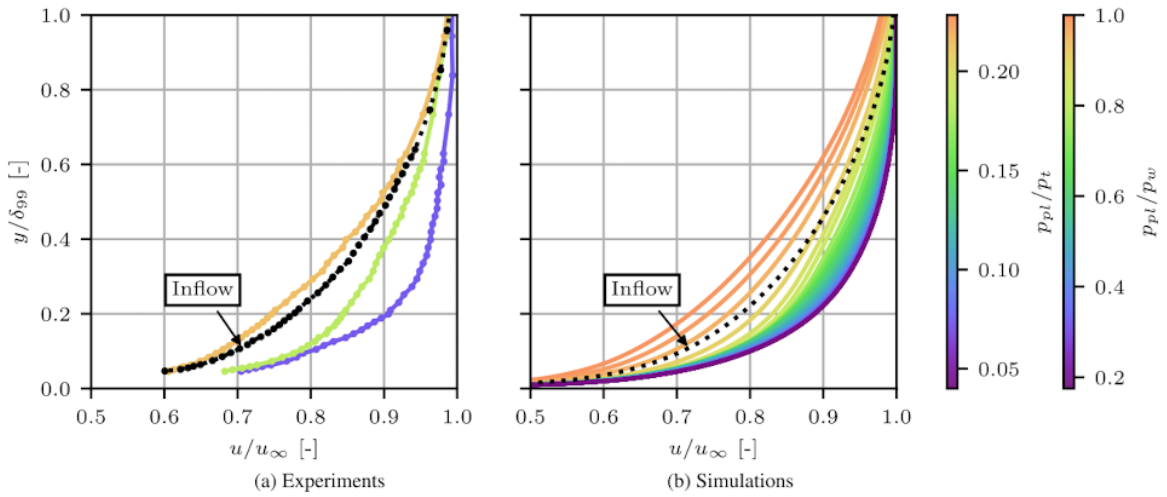


Fig. 1.8 Displacement thickness reduction as a function of plenum pressure ratio p_{pl}/p_t for boundary layer profiles 15mm downstream of bleed region on a plate with high Re (HR) [9].

Zuo et al. [10] extended the application of porous bleed to three-dimensional SWBLI configurations involving conical shock interactions. The implemented methodology was performed using the RANS equations with the Spalart-Allmaras (SA) turbulence model, similar to that of Giehler et al. [9]. Their simulations showed that bleed not only suppresses separation but also modifies the structure of secondary vortices and reduces flow non-uniformity in the approach of and aft of the porous bleed region. These results suggest that porous bleed remains effective even in complex flow environments relevant to modern aerospace system applications.

1.2.6 Modeling of Porous Bleed and CFD Approaches

The accurate representation of porous bleed in computational fluid dynamics is a nontrivial problem due to the small scale and complex physics of the flow within individual bleed holes and the unsteadiness of the turbulent shock system. These flows often involve choked conditions, internal shocks, expansion waves, and recirculation, making direct numerical resolution computationally expensive and physically interpretation complex.

To address this challenge, most simulations employ porous boundary conditions that model the aggregate behavior of the bleed region. Slater [11] developed an improved model based on the concept of a sonic flow coefficient, which relates bleed mass flow rate to local pressure ratios of plenum static pressure and surface static pressure. This approach simplifies implementation by eliminating the need to explicitly determine boundary-layer edge properties and reduces the mach regime to 1, which has been shown to produce good agreement with experimental data.

$$W_{sonic-B} = \Phi A_{region} p_B \left(\frac{\gamma}{RT_B}\right)^2 \left(\frac{\gamma+1}{2}\right)^{-(\gamma+1)/2(\gamma-1)} \tag{1.2}$$

Morell [12] proposed a more advanced analytical model, known as the Boundary Layer Adjusted Model (BLAM), which accounts for additional physical effects such as total pressure losses resulting from incoming boundary layers, non-uniform flow distributions, and three-dimensional interactions at the hole opening, such as bleed hole induced shocks and forward and backward mass

flow. Building off of some of the Slater [11] findings, their work demonstrated improved agreement with CFD results compared to earlier models, highlighting the importance of incorporating realistic flow physics into bleed modeling.

With regards to studies on flow in vacuum, rarefied gas dynamics dominate the behavior of a gas at this regime. The work of LeBeau [13] highlights the application of the Direct Simulation Monte Carlo (DSMC) method, as implemented in the DSMC Analysis Code (DAC), for simulating rarefied and transitional flow regimes where continuum assumptions begin to break down. DSMC is a particle-based, statistical method in which the gas is modeled as a large number of simulated molecules that move, collide, and exchange energy over discrete time steps. Unlike conventional CFD approaches that solve the Navier–Stokes equations, DSMC directly resolves molecular motion and collisions, making it particularly well-suited for high-altitude, low-density flows. In the DAC framework, the computational domain is discretized into cells that are small relative to the local mean free path, λ, ensuring that collisions remain physically meaningful and spatially localized. Within each time step, particles are first moved deterministically according to their velocities, after which intermolecular collisions are computed probabilistically using models such as the variable hard sphere (VHS) or variable soft sphere (VSS) models.

The DAC implementation follows a structured sequence that couples particle motion with macroscopic property evaluation. Boundary conditions are applied through particle–surface interactions, where molecules may reflect diffusely, specularly, or with energy accommodation depending on wall properties. After particle movement and collision steps, macroscopic flow quantities, such as density, velocity, temperature, and pressure, are obtained by sampling particle statistics within each cell. This averaging process allows DSMC to recover continuum quantities while still capturing non-equilibrium interactions such as velocity slip, temperature jump, and shock structure broadening. LeBeau's [13] work emphasizes that the DAC methodology is particularly effective in regimes characterized by moderate to high Knudsen numbers, where traditional continuum solvers struggle. As a result, DSMC via DAC provides a high-fidelity tool for analyzing flows involving strong gradients, rarefaction effects, or complex gas–surface interactions, complementing continuum CFD approaches in aerospace applications [14].

Despite these developments, significant challenges remain. Empirical models may not generalize well across different flow conditions, and high-fidelity simulations that resolve individual holes are often impractical for large-scale studies. These limitations are particularly relevant for nozzle applications, where flow conditions differ substantially from those in inlet systems.

1.2.7 Research Gap and Motivation

Although porous bleed has been widely studied and successfully applied in supersonic inlet design, its use within rocket nozzles has received relatively little attention. This gap is particularly notable given the similarities in SWBLI behavior between inlets and nozzles, as well as the potential benefits of bleed in reducing separation and unsteadiness.

However, several key differences complicate the direct application of inlet bleed concepts to nozzles. In nozzles, the flow is accelerating rather than decelerating, and the pressure gradients are oriented differently. Additionally, the operating environment may involve near-vacuum conditions, leading to potential rarefaction effects in the bleed jet regions. This may necessitate the use of alternative modeling approaches such as Direct Simulation Monte Carlo (DSMC).

Furthermore, the performance metrics for nozzles differ from those of inlets. While inlets

prioritize pressure recovery and flow stability, nozzles must balance separation control with thrust efficiency. The removal of mass through bleed introduces a direct performance penalty, making it essential to quantify trade-offs between flow control effectiveness and propulsion efficiency.

1.2.8 Summary and Research Position

The literature clearly establishes SWBLI/SBLI as a dominant mechanism governing separation and unsteadiness in high-speed internal flows. Extensive research has been conducted on the physics of SBLI and its impact on propulsion systems, particularly in supersonic inlets. Among various control techniques, porous bleed has emerged as one of the most effective methods for mitigating separation.

However, the application of porous bleed to rocket nozzles remains largely unexplored. Existing studies provide valuable insights into SWBLI behavior and bleed mechanisms but do not address the unique challenges associated with nozzle environments. This includes the effects of flow acceleration, vacuum conditions, and propulsion performance constraints.

The present work addresses this gap by investigating the feasibility of downstream porous bleed for SBLI control in rocket nozzles. By combining established bleed concepts with nozzle-specific flow physics, the study aims to advance both theoretical understanding and practical design methodologies for high-performance propulsion systems.

1.3 Project Proposal

The proposed central objective is to evaluate whether downstream porous bleed can reduce the pressure distribution and envelope footprint of an oblique shock generated by a compression corner in a diverging rocket nozzle wall.

This project proposes a computational fluid dynamics (CFD) study of shock–boundary-layer interaction mitigation inside a supersonic rocket nozzle using downstream porous bleed (pressure-relief holes exposed to the environment). A concave compression corner along the divergent nozzle wall will be used to intentionally generate an oblique shock. The study will evaluate whether a porous region placed downstream of this corner can weaken, relocate, or suppress the resulting internal shock structure and associated boundary-layer separation. The project adapts established supersonic inlet bleed-control concepts to a rocket nozzle environment, with particular attention on vacuum-representative operating conditions relevant to space-related propulsion systems. From this, some specific objectives include, but are not limited to:

- Establishing a validated CFD baseline of shock formation in a nozzle with a geometric corner,
- Quantifying shock strength (pressure ratio, angle, wake-area) and separation characteristics,
- Performing a study of bleed porosity, hole size, spacing, and wake length,
- Assessing boundary-layer modification through displacement thickness.

1.4 Methodology

The study will implement compressible Navier-Stokes computational-fluid dynamics modeling to simulate a quasi-two-dimensional axisymmetric converging-diverging nozzle at varying configurations of the same base geometry. Geometry variations are congregated into two cases that vary total porosity independently; where the number of bleed holes is manipulated but the hole

diameter is maintained, and where the bleed hole diameter is manipulated but the number of bleed holes is maintained.

ANSYS Fluent, a commercially off-the-shelf fluidic engineering analysis software, will be used to carry out the entirety of fluid computation segments for this project. Given the supersonic flow behavior rocket engine mechanics require, the SST k-ω turbulence model is used throughout the geometry configuration trials.

A porous-wall boundary condition will model the bleed region, allowing controlled mass removal based on local pressure assumptions in the shock structure. Selected higher-fidelity simulations may resolve individual holes to validate porous modeling trends as a final mature validation. From the data produced by the flow models, behaviorally trends are then analyzed to better illiterate the impact configurations impart to chosen evaluation metrics relative to each other. Some preliminary evaluation metrics include:

- Wall pressure distribution and peak p_2/p_1,
- Displacement thickness, δ^*

The project will continue by extending the geometry and subsequent computational volume into three-dimensions (3D). The porous bleed region of the three-dimensional configuration will be designed as a function of the learned-trends resulting from the proceeding quasi-two-dimensional geometry flows.

The internal nozzle flow is expected to remain in the continuum regime; however, flow exiting from bleed holes into near-vacuum conditions may approach transitional or slip-flow behavior.

2 Fluid Flow Mathematical Framework

2.1 Mathematical Formulation

The present study concerns the numerical modeling of SBLI and its control using porous bleed in a supersonic rocket nozzle. The mathematical framework is therefore based on compressible fluid mechanics, turbulent boundary-layer theory, shock relations, and porous bleed modeling. The governing equations are then for a compressible, viscous, Newtonian gas under the continuum assumption. This assumption is justified when the characteristic length scale of the nozzle and boundary layer remains much larger than the molecular mean free path, such that the Knudsen number is sufficiently small within the supersonic region.

2.2 Continuum Assumption and Knudsen Number

The applicability of the Navier–Stokes equations depends on the validity of the continuum condition. This condition evaluated using the Knudsen number,

$$Kn = \frac{\lambda}{L}, \tag{2.1}$$

where λ is the molecular mean free path and L is a characteristic macroscopic length scale, such as the nozzle throat radius, boundary-layer thickness, or bleed-hole diameter. For continuum flow, $Kn \ll 1$, and molecular effects may be represented through macroscopic properties such as viscosity. If Kn becomes large, for example in highly rarefied high-altitude plume regions, particle-based methods such as DSMC may be required instead of continuum CFD.

For the internal nozzle-flow region considered in this study, the flow is assumed to remain within the continuum regime, allowing the use of the compressible Navier–Stokes equations.

2.3 Governing Equations

The flow field is governed by the conservation equations for mass, momentum, and total energy. In conservative form, the compressible Navier–Stokes equations may be written as

$$\frac{\partial \rho}{\partial t} + \frac{\partial}{\partial x_j}\left(\rho u_j\right) = 0, \tag{2.2}$$

$$\frac{\partial}{\partial t}\left(\rho u_i\right) + \frac{\partial}{\partial x_j}\left(\rho u_i u_j\right) = -\frac{\partial p}{\partial x_i} + \frac{\partial \sigma_{ij}}{\partial x_j}, \qquad i = 1, 2, 3, \tag{2.3}$$

$$\frac{\partial}{\partial t}\left(\rho E\right) + \frac{\partial}{\partial x_j}\left[\left(\rho E + p\right) u_j\right] = \frac{\partial}{\partial x_j}\left(\sigma_{ij} u_i - q_j\right). \tag{2.4}$$

Here, ρ is the density, u_i is the velocity component in the x_i direction, p is the static pressure, E is the total energy per unit mass, σ_{ij} is the viscous stress tensor, and q_j is the heat flux vector [1][6]. These equations form the mathematical basis of CFD simulations for compressible nozzle flows and SBLI.

In a Newtonian fluid, the viscous stress tensor is

$$\sigma_{ij} = \mu \left(\frac{\partial u_i}{\partial x_j} + \frac{\partial u_j}{\partial x_i} \right) - \frac{2}{3} \mu \frac{\partial u_k}{\partial x_k} \delta_{ij}, \tag{2.5}$$

where μ is the dynamic viscosity and δ_{ij} is the Kronecker delta. The heat flux is modeled using

$$q_j = -k \frac{\partial T}{\partial x_j}, \tag{2.6}$$

where k is the thermal conductivity, T is the static temperature, and is as a function of wall distance j.

The gas is assumed to behave as a calorically perfect gas following the ideal gas law,

$$p = \rho R T, \tag{2.7}$$

where R is the specific gas constant. The total energy per unit mass is

$$E = e + \frac{1}{2} u_i u_i, \tag{2.8}$$

with the internal energy defined as

$$e = c_v T. \tag{2.9}$$

2.4 Compressibility Parameters

The compressibility of the flow is characterized primarily by the Mach number,

$$M = \frac{V}{a}, \tag{2.10}$$

where V is the local velocity magnitude and a is the local speed of sound,

$$a = \sqrt{\gamma R T}. \tag{2.11}$$

In a converging-diverging rocket nozzle, the flow accelerates from subsonic conditions in the chamber and converging section to sonic flow at the throat and supersonic flow in the diverging section. The local Mach number determines the character of wave propagation, the formation of shock waves, and consequently the strength of shock-induced adverse pressure gradients.

The Reynolds number is used to characterize the relative importance of inertial flow viscous effects,

$$Re = \frac{\rho V L}{\mu}. \tag{2.12}$$

For boundary-layer analysis, a local Reynolds number may be based on boundary-layer momentum thickness,

$$Re_\theta = \frac{\rho_e U_e \theta}{\mu_e}, \tag{2.13}$$

where U_e, ρ_e, and μ_e are evaluated at the boundary-layer edge, and θ is the momentum thickness [1].

This form is commonly useful in SWBLI studies because the state of the incoming turbulent boundary layer strongly influences separation propagation and interaction length.

2.5 Turbulence Modeling

Because rocket-nozzle SBLI involves high-Reynolds-number turbulent flow, direct solution of all turbulent scales is generally impractical. The governing equations are therefore commonly solved in Reynolds-averaged or Favre averaged form [10]. For compressible turbulent flow, density-weighted Favre averaging is especially useful and is defined as

$$\tilde{\phi} = \frac{\bar{\rho}\bar{\phi}}{\bar{\rho}}, \tag{2.14}$$

where an overbar denotes Reynolds averaging and a tilde denotes Favre averaging.

The Favre-averaged continuity equation is

$$\frac{\partial \bar{\rho}}{\partial t} + \frac{\partial}{\partial x_j}\left(\bar{\rho}\tilde{u}_j\right) = 0. \tag{2.15}$$

The Favre-averaged momentum equation is

$$\frac{\partial}{\partial t}\left(\bar{\rho}\tilde{u}_i\right) + \frac{\partial}{\partial x_j}\left(\bar{\rho}\tilde{u}_i\tilde{u}_j\right) = -\frac{\partial \bar{p}}{\partial x_i} + \frac{\partial \tilde{\sigma}_{ij}}{\partial x_j} - \frac{\partial}{\partial x_j}\left(\bar{\rho}u_i''u_j''\right). \tag{2.16}$$

The additional term,

$$\tau_{ij}^R = -\bar{\rho}u_i''u_j'', \tag{2.17}$$

is the Reynolds stress tensor. This term represents the effect of turbulent velocity fluctuations on the mean flow and introduces the closure problem. In practical CFD simulations, this closure is provided by a turbulence model such as the Spalart–Allmaras (SA) model, the k–ω SST model, or another RANS model.

A common eddy-viscosity approximation is

$$-\bar{\rho}u_i''u_j'' = \mu_t\left(\frac{\partial \tilde{u}_i}{\partial x_j} + \frac{\partial \tilde{u}_j}{\partial x_i}\right) - \frac{2}{3}\bar{\rho}k_t\delta_{ij}, \tag{2.18}$$

where μ_t is the turbulent eddy viscosity and k_t is the turbulent kinetic energy. This approach is widely used because it reduces the cost of turbulent-flow prediction while still allowing the major features of the mean separated flow to be captured.

2.6 Boundary-Layer Quantities

Since SBLI is governed by the response of the near-wall boundary layer to an imposed pressure rise, several integral boundary-layer quantities are important. The boundary-layer thickness δ^* is defined by Anderson [1] as the wall-normal distance for;

$$u(y = \delta) = 0.99U_e. \tag{2.19}$$

The displacement thickness is

$$\delta^* = \int_0^{y_1} \left(1 - \frac{\rho u}{\rho_e U_e}\right) dy \qquad \delta \leq y_1 \to \infty, \tag{2.20}$$

and the momentum thickness is

$$\theta_{MT} = \int_0^{y_1} \frac{\rho u}{\rho_e U_e} \left(1 - \frac{u}{U_e}\right) dy \qquad \delta \leq y_1 \to \infty. \tag{2.21}$$

The boundary-layer shape factor is

$$H = \frac{\delta^*}{\theta_{MT}}. \tag{2.22}$$

These quantities describe the mass and momentum deficit of the boundary layer. A boundary layer with a large near wall momentum deficit is more vulnerable to separation under an adverse pressure gradient. Porous bleed is intended to modify this near-wall profile by removing low-momentum fluid, thereby increasing the boundary layer's resistance to shock-induced separation.

The skin-friction coefficient is

$$C_f = \frac{\tau_w}{\frac{1}{2}\rho_e U_e^2}, \tag{2.23}$$

where τ_w is the wall shear stress. Separation is indicated by a vanishing or negative wall shear stress,

$$\tau_w = 0 \qquad \text{or} \qquad C_f = 0. \tag{2.24}$$

A region of negative wall shear stress corresponds to local reversed flow and is commonly identified as the separation bubble.

2.7 Shock-Wave Boundary-Layer Interaction

When a supersonic flow encounters a concave corner (compression ramp), the flow is turned toward the wall by a deflection angle θ. This turning process generates an oblique shock wave that emanates from the corner. The upstream Mach number M_1 and the flow deflection angle determine the shock angle β through the classical θ–β–M relation.

The normal component of the upstream Mach number is

$$M_{n1} = M_1 \sin\beta, \tag{2.25}$$

and the pressure ratio across the shock is given by

$$\frac{p_2}{p_1} = 1 + \frac{2\gamma}{\gamma + 1}\left(M_{n1}^2 - 1\right), \tag{2.26}$$

where γ is the ratio of specific heats. This pressure rise occurs over a short streamwise distance and imposes a strong adverse pressure gradient on the boundary layer developing along the nozzle wall.

2.8 Boundary-Layer Response to Shock-Induced Compression

The interaction between the oblique shock and the boundary layer is governed by the response of the near-wall flow to the imposed pressure rise. The adverse pressure gradient associated with the shock is expressed as

$$\frac{dp}{dx} > 0. \tag{2.27}$$

As the boundary layer approaches the interaction region, the streamwise momentum near the wall is reduced due to viscous effects. When the imposed pressure gradient is sufficiently strong, the wall shear stress decreases and may approach zero,

$$\tau_w \to 0, \tag{2.28}$$

indicating incipient separation. In such cases, a separation bubble may form downstream of the corner, bounded by a separated shear layer and followed by a possible reattachment region.

However, depending on the upstream boundary-layer state, Mach number, Reynolds number, and turning angle, the interaction may remain attached. Even in attached cases, the boundary layer experiences significant thickening, distortion, and increased turbulent activity.

2.9 Porous Bleed Modeling

The objective of porous bleed control is to remove low-momentum fluid from the near-wall region before or within the SBLI zone. The bleed surface is commonly represented as a porous boundary condition rather than by resolving every individual hole. This approach is appropriate when the bleed-hole geometry is small relative to the full nozzle domain and the primary interest is the aggregate effect of the bleed region.

As described by Slater [11], the porosity of the bleed region is defined as

$$\Phi = \frac{A_{bleed}}{A_{region}}, \tag{2.29}$$

where A_{bleed} is the total open area of the bleed holes and A_{region} is the surface area covered by the bleed region [11].

The bleed mass flow rate is modeled using a sonic flow coefficient,

$$\dot{m}_{bleed} = Q_{sonic}\dot{m}_{sonic}, \tag{2.30}$$

where Q_{sonic} accounts for losses and non-ideal behavior as the flow turns into and passes

through the bleed holes. The ideal sonic mass flow rate may be written as

$$\dot{m}_{sonic} = \Phi A_{region} p_t \left(\frac{\gamma}{RT_t}\right)^{1/2} \left(\frac{2}{\gamma+1}\right)^{\frac{\gamma+1}{2(\gamma-1)}}, \tag{2.31}$$

where p_t and T_t are the relevant total pressure and total temperature.

The suction velocity at the wall may be obtained from the imposed bleed mass flux,

$$v_w = -\frac{\dot{m}_{bleed}}{\rho_w A_{region}}, \tag{2.32}$$

where the negative sign indicates flow leaving the computational domain through the wall. This modifies the near wall mass and momentum balance and can reduce the size of the separation bubble.

3 Rocket Nozzle Model Geometry and Sizing

3.1 Liquid-Propellant Rocket Engine Basis

A desirable model chosen as a basis for SBLI investigation for this study is one that is applied in contemporary aerospace, applied in the near-vacuum environments, and has a relatively accessible quantity of data to draft a model against. With this, the SpaceX Merlin-1D vacuum-optimized rocket engine is used as the foundation of the investigation in this study. From this, while exact dimensions and performance characteristics are not publicly available (most aerospace-related designs are not), some pertinent information is available that can be extrapolated from given further calculation.

The following dimensions and performance characteristics in Table 3.1 serve as a start for rocket engine sizing for the Merlin-1D rocket engine:

Table 3.1 Merlin-1D Vacuum Specifications [15]

Parameter	**Value**
Throat Area, A_t	0.042 m^2
Nozzle Area, A_e	4.90 m^2
Engine Type	Liquid, gas generator
Propellant	LOX/RP-1
Propellant Mix	2.38
Chamber Pressure, P_c	10.8 MPa
Thrust, F_{vac} (vacuum)	981 kN
Specific Impulse, Isp (vacuum)	348 s
Nozzle Expansion Ratio, ϵ_e	165:1

Given the provided data cannot be considered as complete, it serves as a foundation for further engine specification derivation used in this study and which will not stand as an exact representation of the Merlin-1D vacuum engine. Though, from this we continue to derive a model's dimensions next.

3.2 Liquid-Propellant Rocket Engine Geometry Formulation

The geometry for the model used in this study is calculated using historic rocket engine design sizing, in conjunction with the aforementioned Merlin-1D vacuum rocket engine. In utilizing Huzel and Huang's [16] equations in *Modern Engineering for Design of Liquid-Propellant Rocket Engines*, we begin by finding the thrust coefficient:

$$C_f = \frac{F_{vac}}{A_t P_c} = 2.1627. \tag{3.1}$$

We continue by finding the throat and nozzle exit diameters and radii:

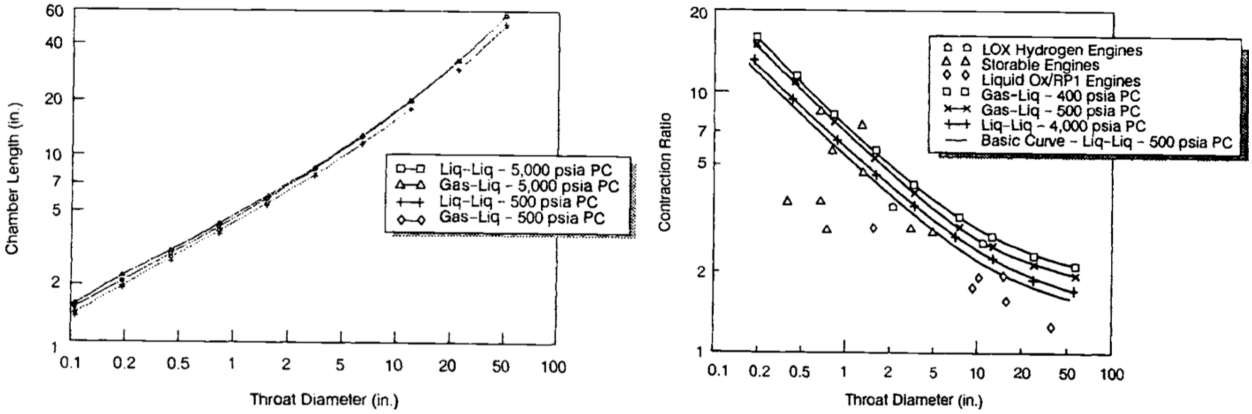
$$D_t = \sqrt{\frac{4}{\pi}A_t} = 0.2312\ m\ (9.1024\ in) \tag{3.2}$$

$$R_t = \frac{1}{2}D_t = 0.116\ m \tag{3.3}$$

$$D_e = \sqrt{\frac{4}{\pi}A_e} = 2.4978\ m \tag{3.4}$$

$$R_e = \frac{1}{2}D_e = 1.2489\ m \tag{3.5}$$

From this, the sizing of the chamber length, L_c, and chamber contraction ratio, ϵ_c, are found from relations used in the scaling program of a LOX/RP-1 liquid rocket engine from Huzel and Huang [16] in the following figures to be $L_c = 0.4318$ m (17 in) and $\epsilon_c = 1.8$.



(a) Chamber length relationships used in scaling program.

(b) Contraction ratio relationships used in scaling program.

Fig. 3.1 Chamber relations from throat diameter [16, p.73].

Given the throat area, the cylindrical chamber area cylindrical chamber radius and diameter are found,

$$A_c = \epsilon_c A_t = 0.756\ m^2 \tag{3.6}$$

$$R_c = \sqrt{\frac{A_c}{\pi}} = 0.1551\ m \tag{3.7}$$

$$D_c = 2R_c = 0.3112\ m \tag{3.8}$$

Next the chamber volume is sized from the typical combustion chamber characteristic length, L^*, of the LOX/RP-1 propellant mix in Fig. 3.2 and Equation 3.9.

From this, it is approximated that $L^* = 1.142$ m (45 in).

$$V_c = L^* A_t = 0.0480\ m^3 \tag{3.9}$$

We know that the Merlin-1D engine has a bell-shaped nozzle, which for this study we can use a half-angle of $a_1 = 20°$ and an upstream contour arc relation as follows;

Table 3.2 Typical Combustion Chamber Characteristic Length (L^*) for Various Propellant Combinations [16]

Propellant Combination	**Combustion Chamber Characteristic Length L^* [in]**
Chlorine trichloride/hydrazine-base fuel	20-35
Liquid fluorine/hydrazine	24-28
Liquid fluorine/liquid hydrogen (GH_2 injection)	22-26
Liquid fluorine/liquid hydrogen (LH_2 injection)	25-30
Hydrogen peroxide/RP-1 (including catalyst bed)	60-70
Nitric acid/hydrazine-base fuel	30-35
Nitrogen tetroxide/hydrazine-base fuel	30-35
Liquid oxygen/ammonia	30-40
Liquid oxygen/liquid hydrogen (GH_2 injection)	22-28
Liquid oxygen/liquid hydrogen (LH_2 injection)	30-40
Liquid oxygen/RP-1	40-50

$$R_U = 1.5R_t = 0.174\ m, \tag{3.10}$$

and subsequently the convergent cone chamber length, L_{n1}, and convergent cone chamber volume, V_n, are calculated [16, p.75,82];

$$L_{n1} = \frac{R_t(\sqrt{\epsilon_c} - 1) + R_U(\sec a_1 - 1)}{\tan a_1} = 0.140\ m \tag{3.11}$$

$$V_n = \frac{\pi}{3} L_{n1}(R_c^2 + R_t^2 + R_c R_t) = 0.0082\ m^3. \tag{3.12}$$

Then, the required cylindrical chamber volume, V_{req}, and required cylindrical chamber length, L_{req} can be calculated as

$$V_{req} = V_c - V_n = 0.0398\ m^3 \quad and \tag{3.13}$$

$$L_{req} = \frac{V_{req}}{\epsilon_c A_t} = 0.526\ m, \tag{3.14}$$

where then the injector-throat length, L_T, is found as

$$L_T = L_{req} + L_{n1} = 0.666\ m. \tag{3.15}$$

Once the dimensions of the combustion chamber are found, we can then move forward with downstream/divergent nozzle dimensions. Again, the nozzle used is a conical bell shape, and for the purpose of this study an 80% fractional nozzle length is implemented. With this, the downstream contour radius, R_D, is found along with the divergent nozzle length, L_{n2}, given a half-angle of $a_2 = 15°$:

$$R_D = 0.382R_t = 0.0443\ m \tag{3.16}$$

$$L_{n2} = 0.8\frac{R_t(\sqrt{\epsilon_e} - 1) + R_D(\sec a_2 - 1)}{\tan a_2} = 4.1071\ m \tag{3.17}$$

Next, the initial (neck) and final (exit) parabolic angles, θ_n and θ_e, of the diverging nozzle are approximated as a function of exit expansion ratio, ϵ_e, from the relation in Figure 3.2.

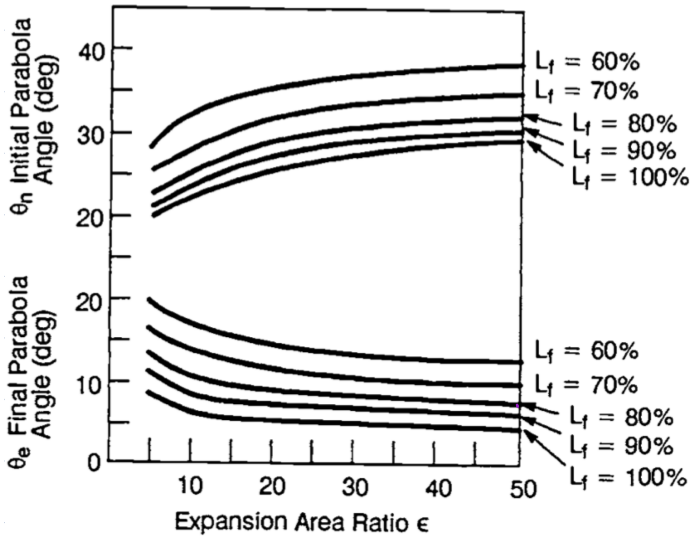


Fig. 3.2 Divergent neck, θ_n, and exit parabolic, θ_e, angles as a function of expansion area ratio [16].

With approximate angles of $\theta_n = 27°$ and $\theta_e = 9°$, the diverging nozzle-throat distance, N_t, and diverging nozzle-throat radius, N_a, are found as

$$N_t = 0.382R_t \sin\theta_n = 0.02011\ m \quad and \tag{3.18}$$

$$N_a = R_t + 0.382(1 - \cos\theta_n) = 0.12083\ m. \tag{3.19}$$

In following Huzel and Huang's [16] formulation, for completeness the following relation is stated:

$$E_t = L_{n2} \quad and \tag{3.20}$$

$$E_a = R_e. \tag{3.21}$$

The resulting calculated dimensions are used to form the baseline model geometry for the study of internal flow of the rocket nozzle. From the baseline model geometry, adjustments and modifications are made at the nozzle wall to investigate the implementation of porous bleed on a

nozzle with a compression corner and resulting SBLI.

3.3 Computer-Aided Design Model Geometries

From the rocket engine formulation calculations the implementation of computer-aided design software (CAD) is used to model each geometry for further use in flow analysis. SolidWorks is the chosen software to draft the models needed for study. The varying rocket engine nozzles, based off of the Merlin-1D engine design, are then further specialized from the baseline model, which serves as the control configuration to which the concave corner and porous bleed studies are built from.

3.3.1 Control Rocket Nozzle Geometry Configuration

The control rocket nozzle configuration leverages the dimensional values directly from the geometry formulation and are shown in Table 3.3. From this, a visual representation of the geometry dimensions are shown in the following design drawing: Fig. 3.3.

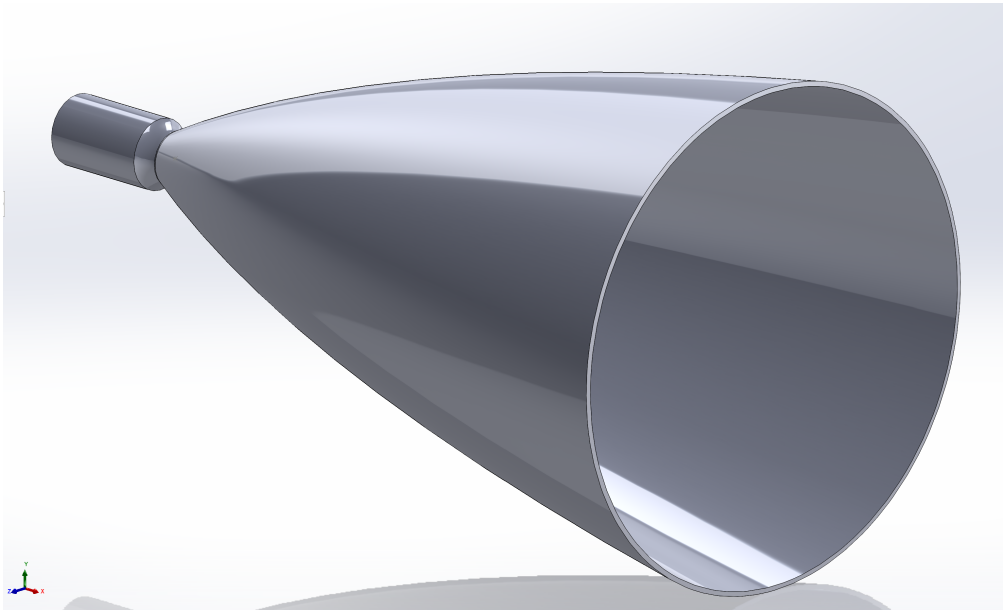


Fig. 3.3 Isometric view of the 3D rocket engine control configuration model.

Additionally, a two-dimensional (2D) solid surface is modeled from the control configuration as preliminary means of study for the flow behavior within the control configuration. Shown in Fig. 3.6 is a the two-dimensional solid surface sliced about the x-axis, reducing the computational volume, and therefore saving on computation requirements during flow simulation.

Table 3.3 Collated Baseline Rocket Engine Characteristics

Dimensional Parameter	Value [unit]
D_t	0.2312 m
R_t	0.1160 m
R_e	2.4978 m
R_e	1.2489 m
A_c	0.7560 m^2
R_c	0.1551 m
D_c	0.3112 m
V_c	0.0480 m^3
R_U	0.1740 m
L_{n1}	0.140 m
V_n	0.0082 m^3
V_{req}	0.0398 m^3
L_{req}	0.526 m
L_T	0.666 m
L_{n2}	4.1071 m
N_t	0.0201 m
N_a	0.1208 m
θ_n	27 °
θ_e	9 °

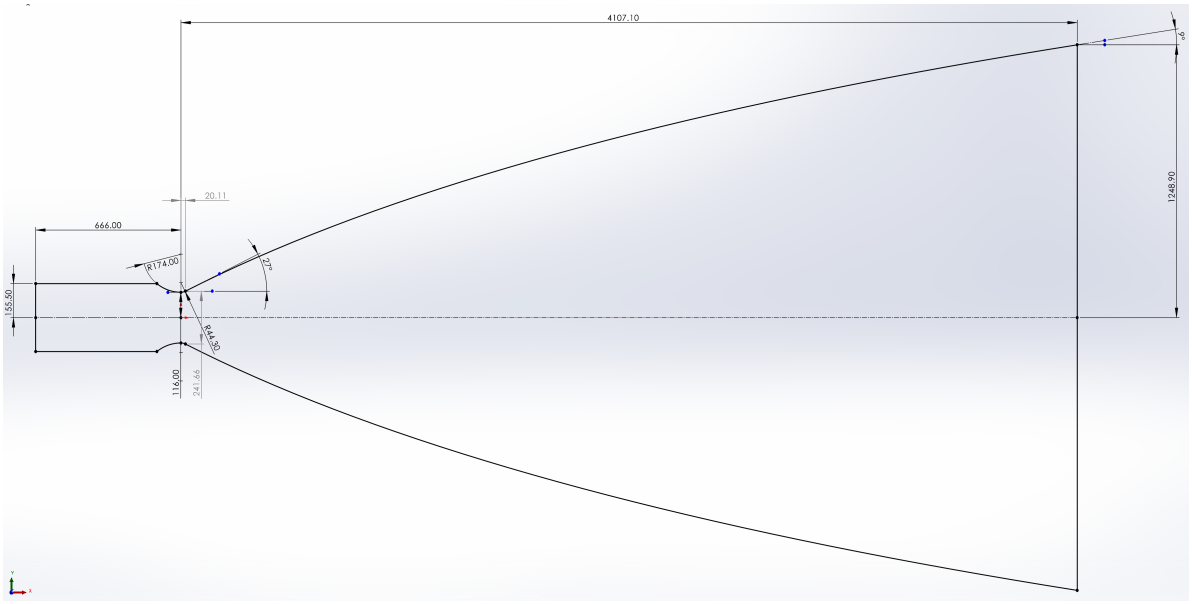


Fig. 3.4 Full view of the rocket engine control configuration design sketch in [mm].

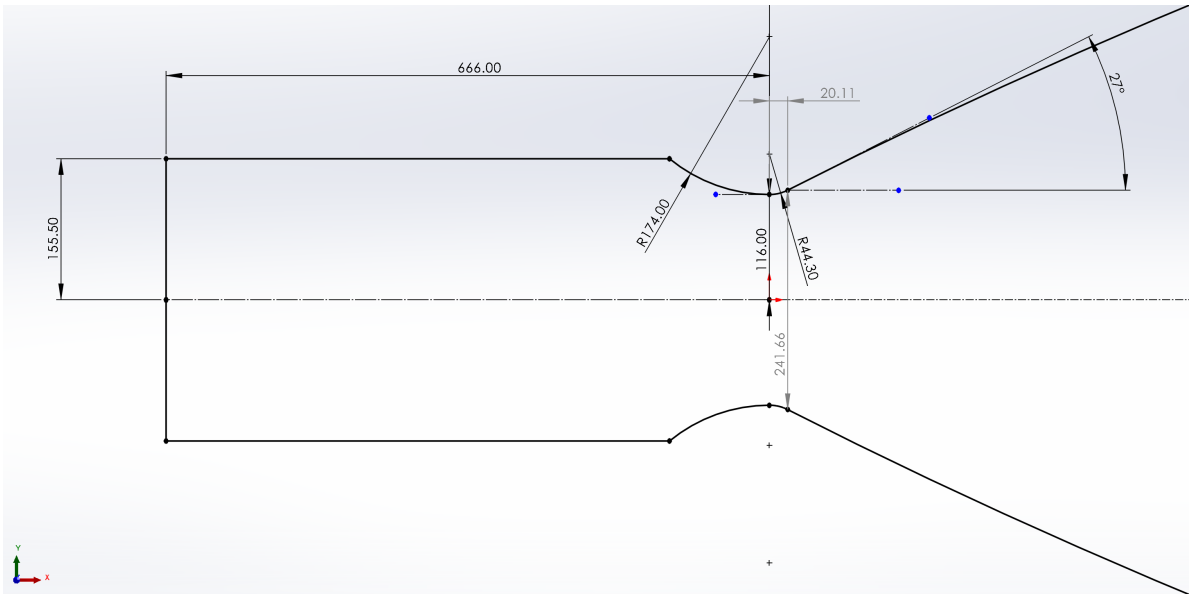


Fig. 3.5 Zoomed view of the rocket engine control configuration design sketch in [mm].

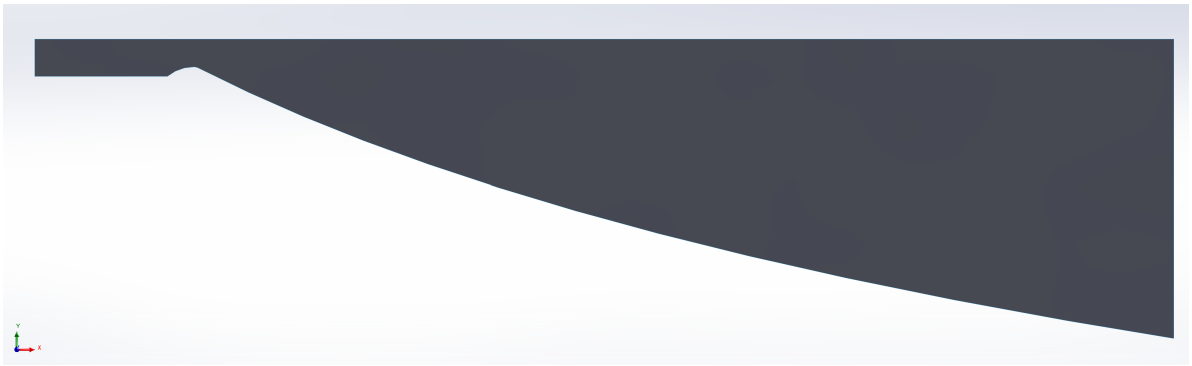


Fig. 3.6 2D symmetric solid surface of the rocket engine control configuration.

3.3.2 Concave Corner Rocket Nozzle Geometry Configuration

A concave compression corner is implemented to generates a desired shockwave and post-shock region. This region has the nozzle wall parallel along the x-axis and meets with the parabolic curve of control nozzle wall geometry to create the corner structure.

At a distance of 1000 millimeters from the nozzle exit, the resulting deflection angle of the imposed ramp results to 11.1° from tangent of the parabolic curved nozzle wall, pre-shock region, shown in Fig 3.7.

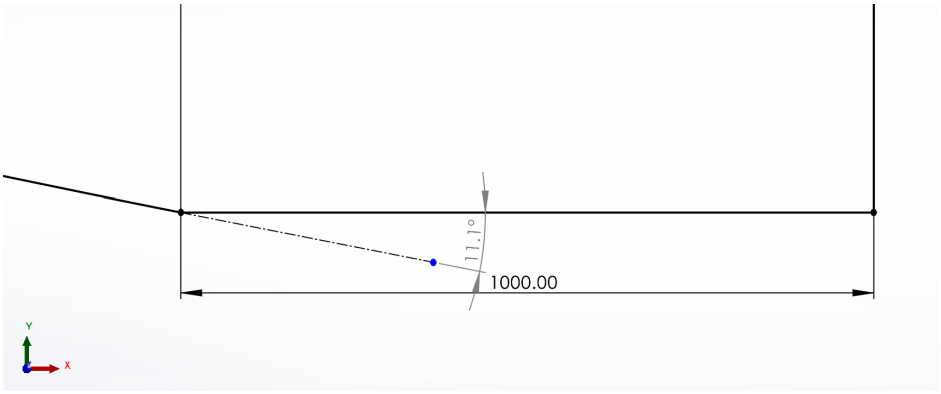


Fig. 3.7 Schematic of concave compression corner at 11.1° ramp angle.



Fig. 3.8 Solid Surface of concave compression corner at 11.1° ramp angle.

3.3.3 Porous Bleed Region Geometry Configurations

The porous bleed region is comprised of bleed holes that vary in number. For the first set of bleed hole configurations, the diameter of the holes are kept constant at 25 mm. Shown in Fig. 3.9, this first set of configurations prescribe the geometries have 4 bleed holes, 8 bleed holes, and 12 bleed holes, respectively.



(a) 4-hole configuration. (b) 8-hole configuration. (c) 12-hole configuration.

Fig. 3.9 Porous bleed region with varying bleed hole number configurations with identical diameters of 25 mm; a) 4 symmetric holes, b) 8 symmetric holes, c) 12 symmetric holes.

The next set of bleed hole configurations the number of holes is kept constant, while the diameter of each hole is varied between configuration geometries. The number of holes chosen, 25, is so based off the performance results from the previous set of geometry configurations. In

essence, the second set of geometry configurations builds off of the first set of geometries given the favorable behavior presented and described in later sections.



(a) 5 mm bleed hole diameter. (b) 10 mm bleed hole diameter, (c) 15 mm bleed hole diameters.

Fig. 3.10 Porous bleed region with varying bleed hole diameter configurations with constant 25 hole number; a) 5 mm bleed hole diameter, b) 10 mm bleed hole diameter, c) 5 mm bleed hole diameter.

For both sets of geometries, the bleed hole placement is kept equidistant with respect to each other and from the range boundaries of the shock region; where the compression ramp begins to where the compression ramp ends (or the outlet of the rocket nozzle).

3.3.4 Three-Dimensional Model Geometry Configuration and Considerations

To further the study of SBLI mitigation using porous bleed a three-dimensional geometry model is designed with a three-dimensional flow simulation in consideration. The volume geometry builds off of the same dimensions as the preceding two-dimensional concave corner case, but revolved 90° around the central axis.

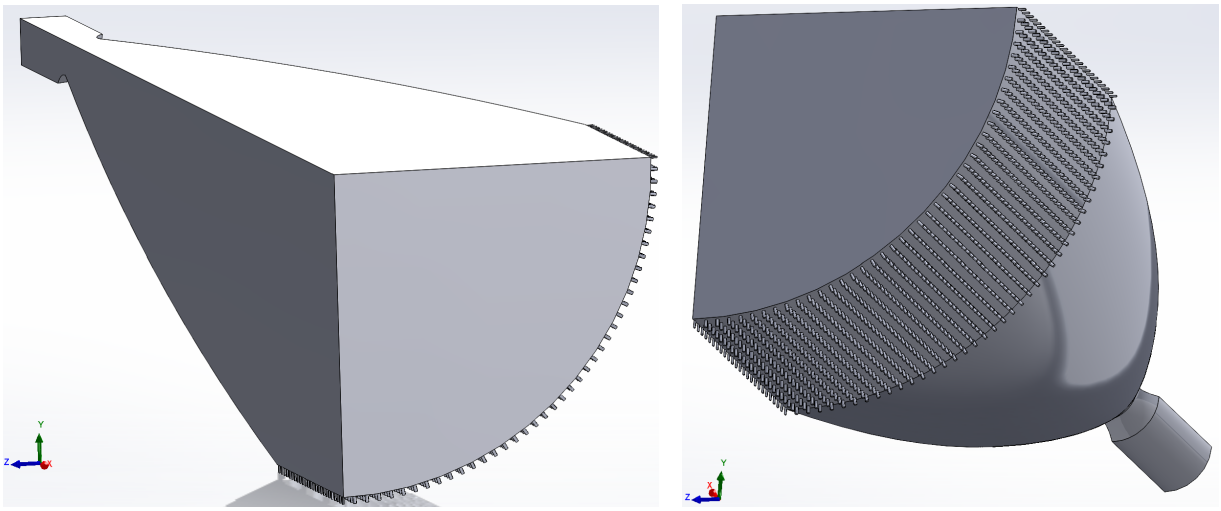


Fig. 3.11 Axisymmetric 3D model with 1050 bleed outlets in square-grid in bleed region at one-quarter volume.

The chosen geometry is revolved by 90° instead of a full 360° to produce 25% of the original volume. Given the rocket engine is axisymmetric, the same assumption of symmetry applied in the quasi-two-dimensional case is also applied to the three-dimensional case in efforts to save in

computational requirements, save on time to run multiple CFD trial simulations, and stay within ANSYS Fluent Student License node/element limits during the meshing process.

This geometry departs from the two-dimensional scenarios by arrangement of bleed holes in the porous region. Through analyzing the results of varying hole quantity and hole diameter demonstrate in the two-dimensional bleed geometries, the three-dimensional model has the bleed holes lining the circumference of the porous region wall in a 25 x 42 rectangular-grid configuration, resulting in a total of 1050 bleed hole outlets in the quarter-section of the bleed region. A hole diameter of 10 mm permits a balance between pressure ratio and displacement distance reduction and inter-hole gap preservation; a facet of porosity intended for examination during later analysis.

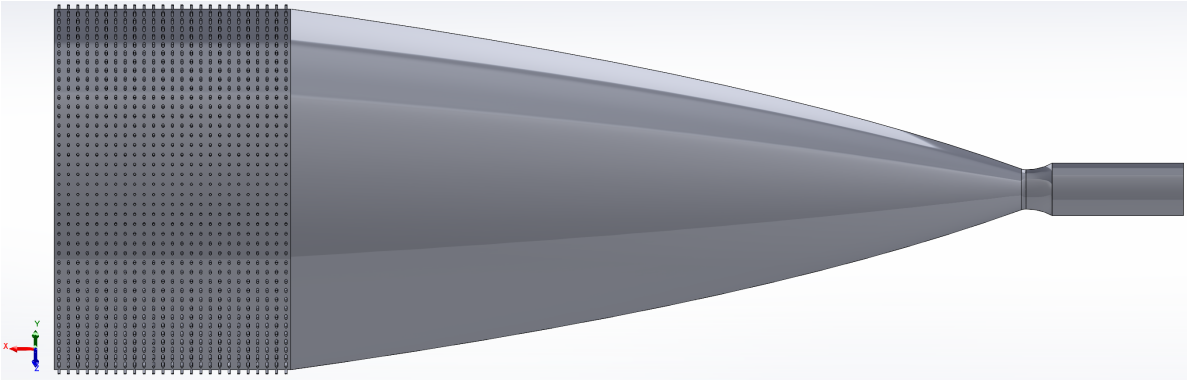


Fig. 3.12 Axisymmetric 3D model with porous bleed region and full-length rocket engine volume.

The three-dimensional model, like the two-dimensional case, preserves the full-length rocket engine (from the inlet injector face to the outlet nozzle face) to maintain consistency between previous geometry permutations and preserve the flow physics and performance of the Merlin-1D vacuum rocket engine this study adapts its models. Like the preceding geometries, the hole depths are maintained at 25 mm for consistency and allow for enough volume for hole-edge behavior to be studied and enough distance between the nozzle interior and outlet boundaries to ideally capture the physics of outward mass flux to the flow.

4 Numerical Computation Setup

4.1 Mesh Generation for Solid Model Geometries

The study of porous bleed as a method for flow control and manipulation in SBLI flows is first carried out in a two-dimensional configuration to study the performance resulting from a simplified environment. Once the behavior of the two-dimensional configuration is established, the study is further extrapolated to encompass three-dimensional model configurations when more complex behavior is expected arise.

4.1.1 Model Geometry Meshing for 2D Consideration

The generation of a numerically meaningful mesh is imperative in reflecting physically accurate results from a CFD flow simulation. From the two-dimensional surface model of the control configuration, the surface is further broken up into four more surfaces before the mesh is generated: from engine well injection to the start of engine converging region, through the engine converging region to the engine throat, from the engine throat through the engine diverging region, and finally from the end of the engine diverging region through the diverging nozzle to the nozzle exit. The described regions are shown in alternating order from left to right in Fig. 4.1.

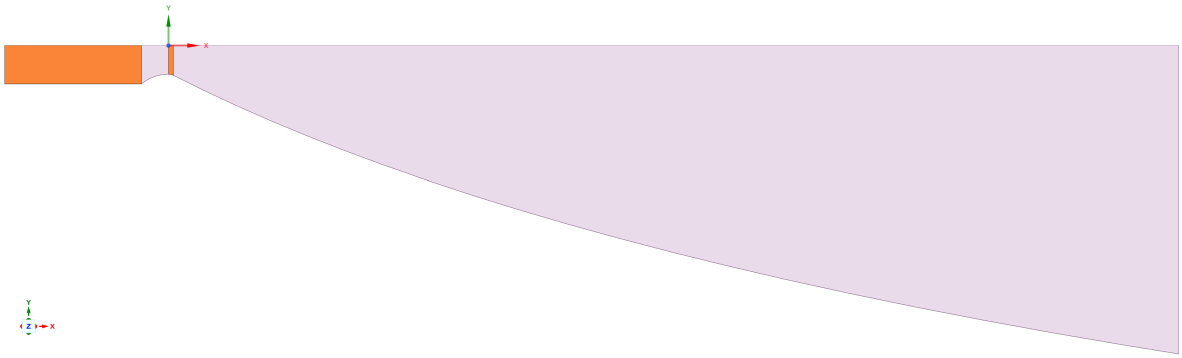


Fig. 4.1 Full view of the 2D symmetric solid surface regions of the control configuration.

The rocket engine surface domain is partitioned into distinct regions to allow for the generation of a structured mesh, opposed to an unstructured mesh. Briefly, a structured mesh is preferable compared to a unstructured one because the cells/nodes produced yield greater numerical control and accuracy for the same geometry. The advantages of a structured mesh are present in increased resolution of boundary-layers, lowered numerical diffusion (where cells/nodes align favorably along supersonic flor streamlines), increased accuracy in gradients in flow, increased computational efficiency (computation time is decreased dramatically), and quicker convergency behavior [17]. Structured meshes of the control configuration model are shown in Fig. 4.2 and Fig. 4.3.

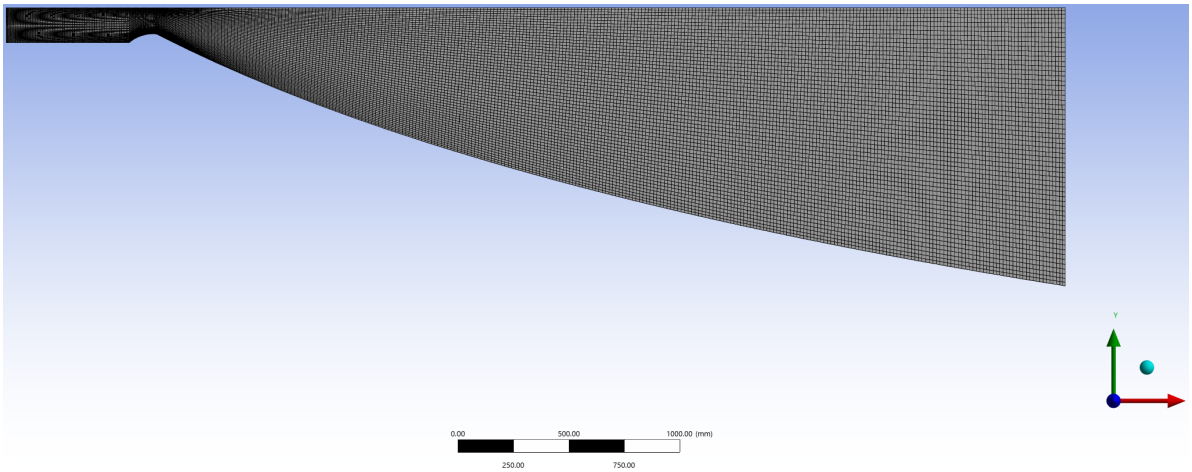


Fig. 4.2 Full view of the 2D symmetric mesh of the control configuration.

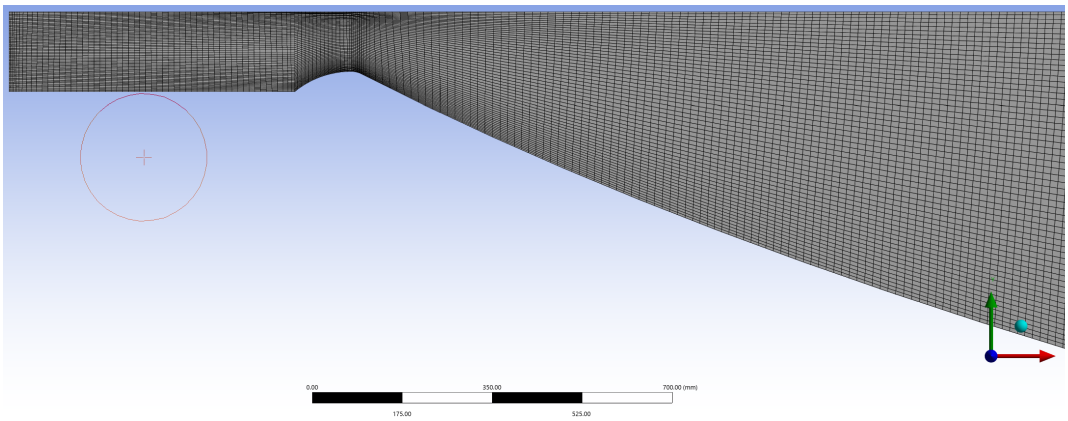


Fig. 4.3 Zoomed view of the 2D symmetric mesh of the control configuration.

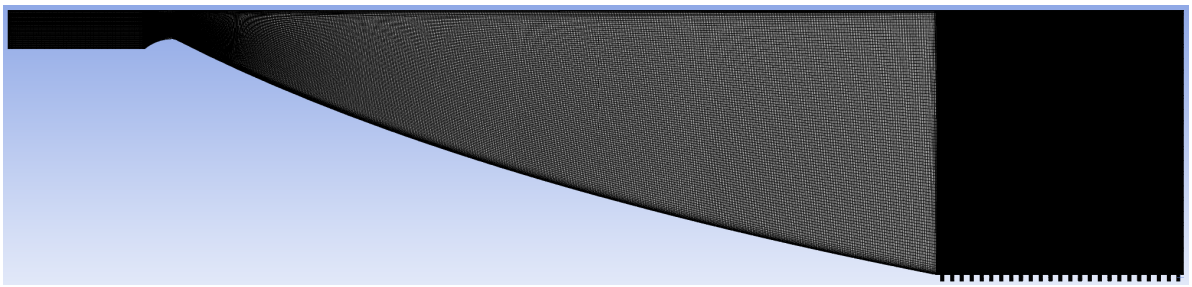


Fig. 4.4 Full view of the 2D symmetric mesh of the variable diameter 15 mm configuration.

Given the desired benefits of a structured mesh, the number of divisions both in the x- and y-axes are defined directly for all two-dimensional simulations. In light of element and node size limitations, the structured mesh grid elements and nodes aim to follow the streamlines of the internal fluid flow, while increasing resolution in areas of particularly important study, such as the porous region where the oblique shockwave is intended to manifest, which can be seen in Fig.

4.4 below. As Yang et. al. showed around their work involving a grid independence test, mesh refinement around the regions of study yield advantageous results in reducing error for calculated performance data [18].

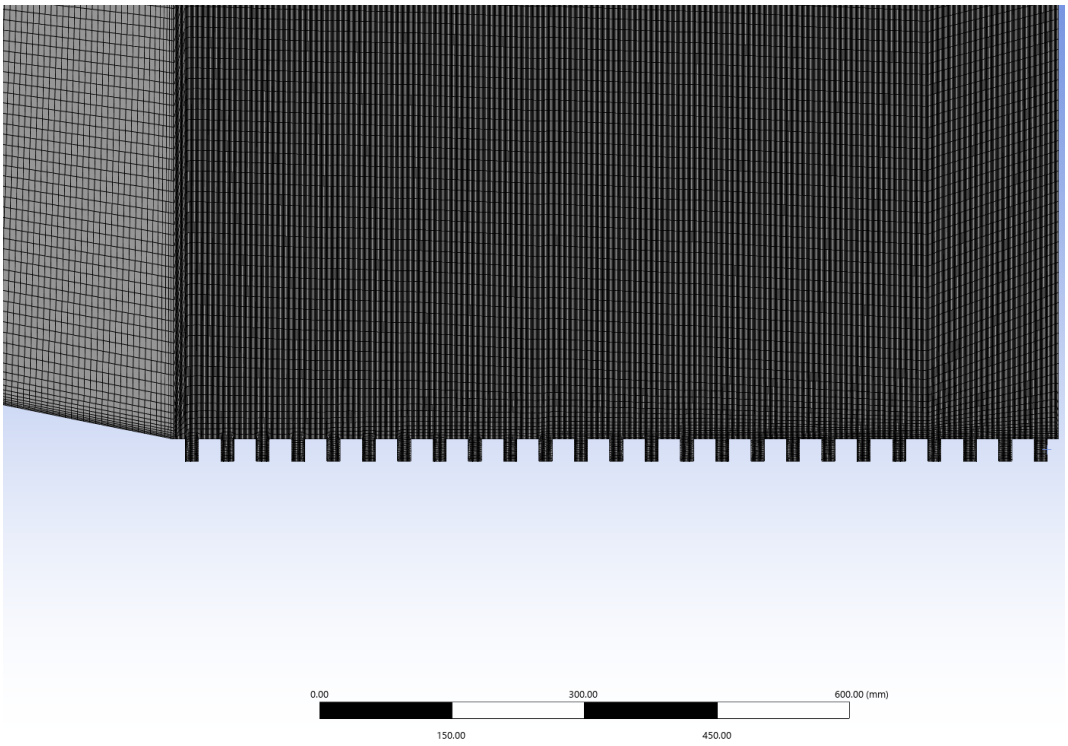
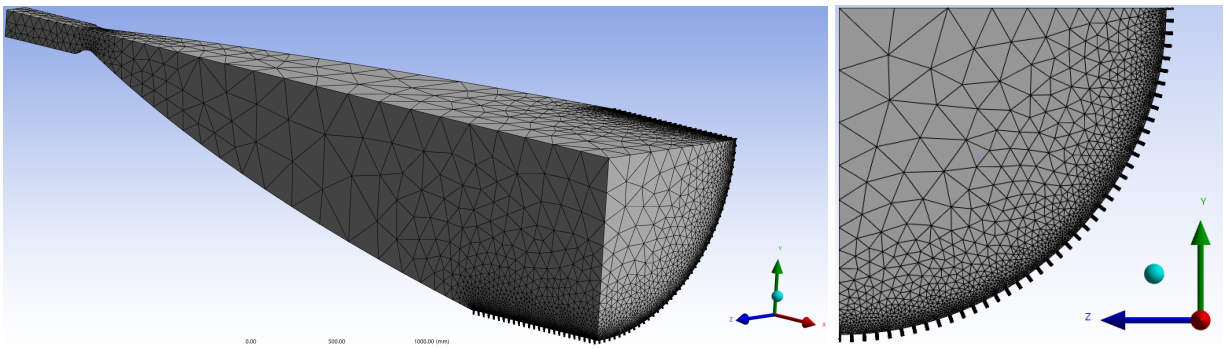


Fig. 4.5 Zoomed view of the 2D symmetric mesh of the variable diameter 15 mm configuration.

Further mesh refinement near the wall and in the region of study is preferable for producing accurate results in the project. A mesh inflation is applied near the nozzle wall along with a more fine cell size in efforts to capture representative flow physics, seen with greater clarity in Fig. 4.5. The bleed region receives additionally refinement by increasing the x-axis divisions compared to those of the upstream cell zones. As a result, the region resolution enables the distinction of localized flow phenomena, particularly around the hole inlet, outlet, and edges, through greater discretization of area.

4.1.2 Model Geometry Meshing for 3D Consideration

Theoretically, the addition of the third spacial dimension increases the number of cells in a computational volume by an order of magnitude when compared to a two-dimensional surface of similar dimensions. The current version of ANSYS Fluent permits an upper limit of 1 million nodes and/or elements for a given mesh of the Student License. This conditions heavily influences the volume resolution and requires greater attention to mesh sizing location and resolution. With a total axial length of 4774.10 mm from injector inlet to nozzle outlet, an equally-sized cell size of the model volume yields elements too large to capture the detail around the porous region, resulting in de-featuring of geometry details most relevant to the project.



(a) Full computational volume of 3D axisymmetric mesh at one-quarter volume.

(b) Outlet near-wall cell size growth.

Fig. 4.6 Three-dimensional mesh with one-quarter volume.

In addition to decreasing the total geometry volume by 75% and simulating around symmetric boundary conditions, further cell size refinement is required to balance mesh resolution with the upper node/element limit. Unfortunately, the most impactful cell zone to cell/element quantity is the porous region. The additional surface area, edge length, and volume of the 1050 bleed holes greatly dominates percentage of cells in the total computational volume. From this, settings that reduced the element size most are as follows [19]: cell Growth Rate sizing increases radially inward from the wall at a rate of 1.26 (default 1.20), the Curvature Minimum Size is increased from 2.50 mm to 6 mm, the Curvature Normal Angle is increased from 18° to 36°, and the Multizone is used for the Sweepable Body Method in efforts to utilize both hexahedral and tetrahedral mesh structures.

As seen in Fig. 4.6, cell resolution increases radially outward at a rate of 1/1.26, drawing greater capture of flow detail closer to the wall boundary. This is preferential given the project's focus on the study of shockwave-boundary-layer interactions.

4.2 ANSYS Fluent Simulations

To carry out the flow study of SBLI and porous bleed, ANSYS Fluent is used as the medium for computational flow study of the following study. The Student Version of ANSYS Fluent is used due to software accessibility, which offers double precision calculation but restricts the number of cores allowable to 4 and the number of cells/nodes to 1 million, impacting the precision and computational accuracy of resulting fluid simulations.

Nevertheless, the restriction on cell/node count presents a parameter for consideration, and accommodations are met by reducing computational volumes about symmetric regions to improve cell count and subsequent model results fidelity.

The environmental operating conditions are set so that they mimic an ambient near-vacuum environment. Additionally, the inlet pressure and inlet temperature are sized by the thrust coefficient, engine geometry, and flow parameters. These preliminary calculations in conjunction with the publicly available baseline data of the Merlin 1D rocket engine form the parameters used throughout the numerous flow simulations.

Table 4.1 Control Configuration Simulation Settings

Setup Settings	**Value**
Energy Equation	ON
Model	Viscous SST k-omega
Solver	density-based
Transience	steady
Materials	Air
Density	ideal-gas
Operating Pressure	0.032 Pa
Solution Methods	
Formulation	Implicit
Gradient Spacial Discretization	Green-Gauss Node-Based
Flow, k, & omega	Second-Order Upwind
Solution Courant Number	1
Initialization Courant Number	0.75
Solution Number of Iterations	
2D Computational Volume	15,000
3D Computational Volume	2,000
Boundary Conditions	
Inlet Type	pressure-inlet
Inlet Pressure	10.8 MPa
Inlet Temperature	3650 K
Outlet Type	pressure-outlet

All scenario and geometry permutations are carried out nearly identically with regards simulation setup. While the compression chamber, converging section, throat section, and most of the diverging section are not the focus of study, it was decided valuable that the full flow, through the mentioned sections, is included in the analysis and computation of the project. The inlet boundary condition is set to the far left wall of the combustion chamber (physically as the injector head) at a prescribed pressure seen in Table 4.1. For the two-dimensional simulations, a symmetric representation of the entire engine cross section is used, where, the walls are set to a zero-slip wall boundary condition and the central axis of the engine is set to a symmetric boundary condition.

The density-based solver is set for the carried-out simulations because of the compressibility of the flow for the project. Briefly, the density-based solver, in conjunction with the energy equation, is ideal over the pressure-based solver because continuity, momentum, and total energy are solved in parallel rather than solving pressure solely through a separate pressure-correction equation. Additionally, especially for Re computation environments, Edwards found good agreement between hybrid LES-RANS predictions and experimental data, although some slight deviation around the separation region [20], and so Hybrid calculation in ANSYS Fluent is also implemented for this project.

5 Results and Discussion

The following section aims to discuss and analyze the results of the numerous flow simulations carried out for the control concave corner, and porous bleed configurations. We begin by validating the internal flow behavior of the nozzle geometry without a compression concave corner by verification of expected pressure and mach velocity regimes. Once an appropriate internal flow behavior is established for a rocket nozzle, the geometry is modified to further carryout the study. From this, the internal flow of the compression corner configurations without any porous bleed geometry is analyzed to establish pre-shock and post-shock performance metrics. Building from the compression corner geometry, porous bleed geometry is applied in two different variations, holding either hole size or hole prevalence, constant while suspending the other, to study the impact of each set of variations, in isolation of one another, on the prescribed shockwave performance metrics. Lastly, an axisymmetric three-dimensional flow model is analyzed to further understand the shock and bleed behavior given the complexity increase from potential interacting supersonic flow.

5.1 Computational Flow Field Analysis

5.1.1 Control Nozzle Geometry Flow Simulation

The initial set of fluent simulations are run with the simulation parameters shown in Table 4.1. Settings such as the Courant numbers and iterations are varied through the discovery process in efforts to better understand result and convergence behavior of each simulation.

The set of simulations carried out for the two-dimensional symmetric control configuration are intended to establish a baseline of performance metrics demonstrated by the control configuration of the rocket engine model geometry. The idealized values produced reflect the supersonic flow behavior within a vacuum-optimized rocket engine and nozzle.

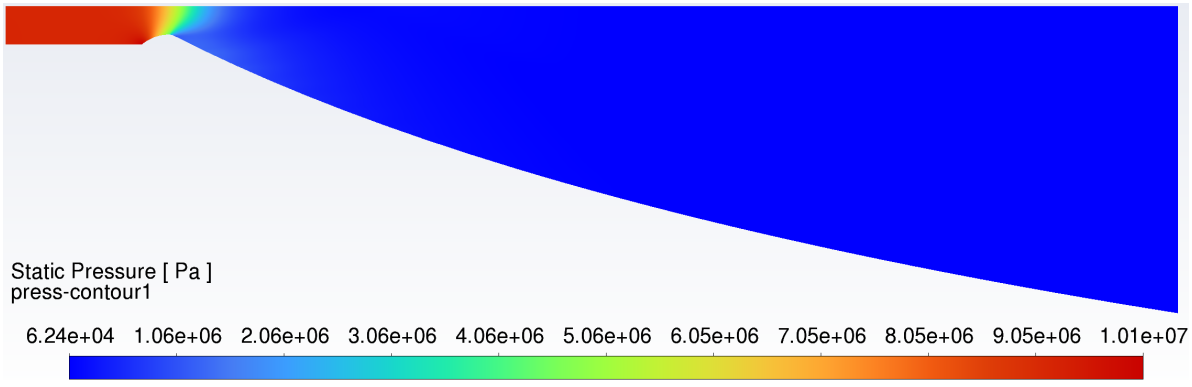


Fig. 5.1 Pressure contour of the 2D symmetric fluent flow.

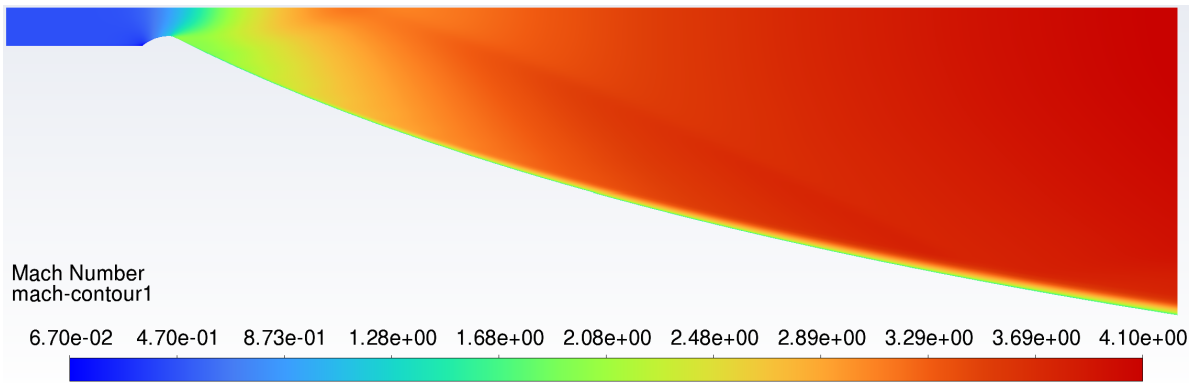


Fig. 5.2 Mach contour of the 2D symmetric fluent flow.

The resulting initial flow simulations align with de Laval nozzle expectations within each region of flow. The mach and pressure contours, shown in Fig. 5.2 and Fig. 5.1 respectively, represent the classical behavior of a converging-diverging nozzle [1]. From the resulting contours, it shows that mach number is lowest in the combustion chamber, increases to Mach 1 at the throat, and further rises to magnitudes greater than 1 or at an approximate maximum of Mach 4. In addition to the velocity rise, the pressure is at the lowest magnitude within the nozzle region, approximately 63 kPa, from the high region within the combustion chamber having an approximate maximum static pressure of 10 MPa, which was a predefined boundary condition for the inlet pressure.

5.1.2 Flow Simulation of Compression Corner without Porosity

A CFD flow simulation of the same initial environmental parameters as the control geometry is conducted for the concave compression corner geometry to generate the shockwave front and subsequent post-shock region that is used for later porous geometries. As discussed in previous sections, the ramp angle of 11.1° is applied so that the post-shock region has the nozzle wall parallel with the net flow velocity vector (parallel with the x-axis). From thus, the region post shock has a range of 1000 mm; from the concave corner to the nozzle outlet.

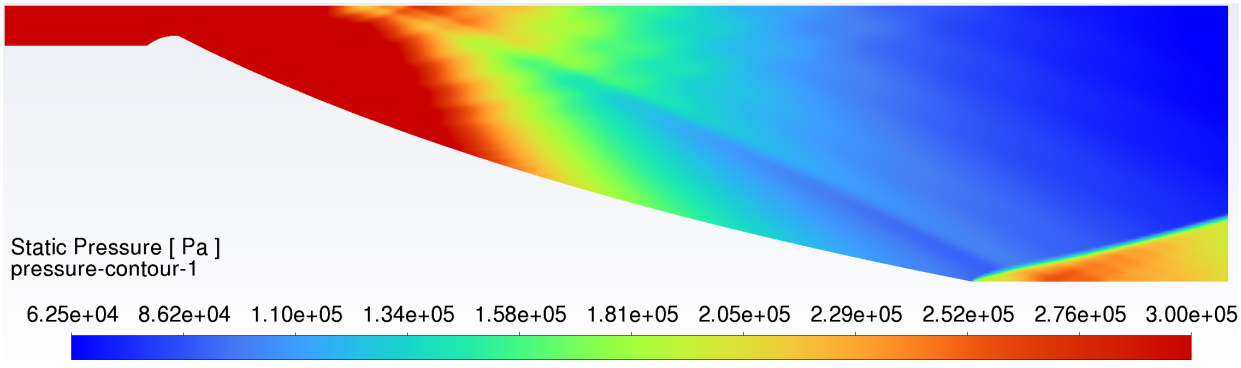


Fig. 5.3 Static pressure distribution of full 2D rocket geometry with compression corner and null porosity.

As can be seen in Fig. 5.3 a post-shock region developed, showing a clear increase in static pressure as a result. The range is set to highlight the magnitude in difference between pre-

and post-shock regions of pressure. For ease of analysis and to highlight the greatest impact on resulting magnitude the project compares performance metrics, such as displacement distance, pressure ratio, etc., at the outlet of the nozzle region. With the greatest distance from the start of the generated oblique shock, the impact of shockwave mitigation mechanisms are largest from greater distance downstream of the shock inception location.

The nozzle outlet is 4773.1 mm from the combustion chamber inlet, 4107.1 mm from the throat, and 1000 mm from the oblique shock start. At the exit the displacement distance, δ^*, is of particular sensitivity due to the pressure equilibrium potential being greatest. Even with this, the it is clear the induced shock is a result of the compression corner and yields a predictable high pressure region, with a peak p_2 pressure of approximately 280 kPa to 300 kPa.

Table 5.1 Local Average and Extrema Pressures along Porous Region Wall, p_2

Geometry Permutation	**Maximum Static Pressure [kPa]**	**Average Static Pressure [kPa]**	**Minimum Static Pressure [kPa]**
No Porous Region	258.5010	225.0403	104.6485
4 Porous Holes	320.6430	209.7116	55.6333
8 Porous Holes	293.4990	187.8517	56.8364
12 Porous Holes	304.8108	182.8047	55.0025
5 mm Holes	300.5855	207.2287	50.8736
10 mm Holes	359.4362	193.0662	41.8769
15 mm Holes	433.1204	179.3719	48.6433

5.1.3 Flow Simulation of Porous Bleed Region with Variation in Hole Quantity

To investigate the impact of bleed hole geometry on SBLI mitigation, the varied geometries are simulated given the same initial environmental conditions as the control and concave compression corner configurations. Holes in the porous bleed region are set to have an outlet pressure boundary condition, the same boundary condition given to the nozzle exit of the control and concave corner geometries.

The first set of bleed region configurations varies the number of identical bleed holes in the post-shock region, shown in Fig. 5.4, Fig. 5.5, and Fig. 5.6. The distance between each hole is kept proportionally the same to reduce variability in longitudinal results.

When viewing the pressure contours for the former set of porous geometries it is clear that the post-shock region yields a predictable high relative pressure to the pre-shock region. Given the same static pressure range, it is evident that average p_2 decreases as porosity increases in light of bleed hole quantity. Seen clearly in Fig. 5.15, localizations of high and low pressures are also observed at both the leading edges and trailing edges of the bleed hole cavities. This behavior is commonly seen for 90° hole configurations in presence of supersonic flow regimes [12].

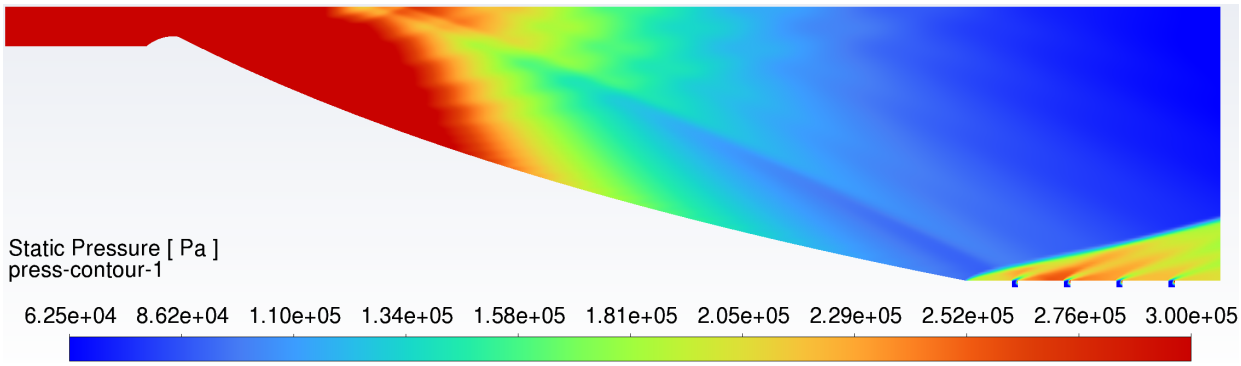


Fig. 5.4 Static pressure distribution of full 2D rocket geometry with porous bleed region at a 4-hole configuration of 25 mm diameter.

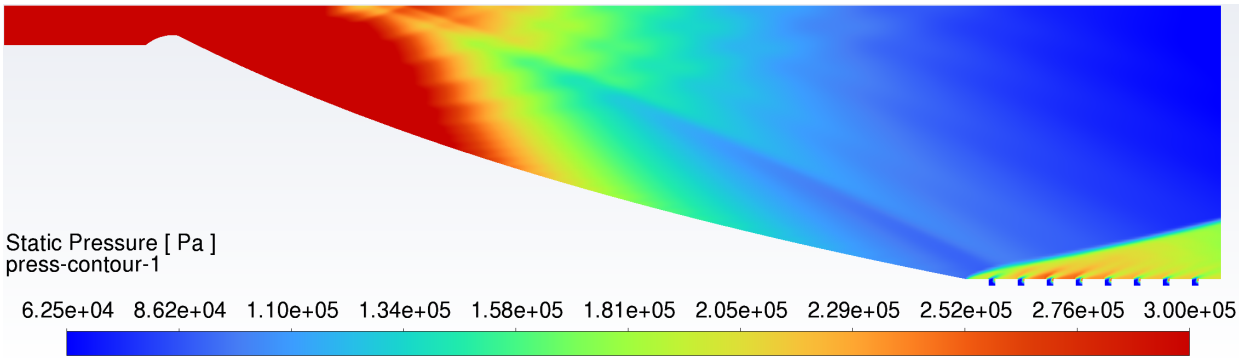


Fig. 5.5 Static pressure distribution of full 2D rocket geometry with porous bleed region at a 8-hole configuration of 25 mm diameter.

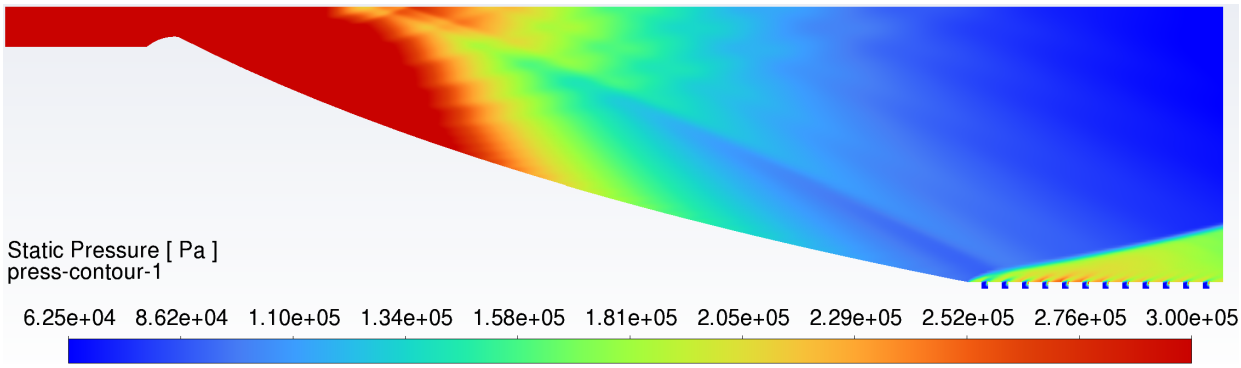


Fig. 5.6 Static pressure distribution of full 2D rocket geometry with porous bleed region at a 12-hole configuration of 25 mm diameter.

5.1.4 Flow Simulation of Porous Bleed Region with Variation in Hole Diameter

The next set of bleed region configurations varies the diameter of the bleed holes in each region, while maintaining the overall number of holes constant. The holes are equally spaced

within the 1000 mm post-shock region and also have the same height from the internal nozzle wall to the outlet surface, along with the same exit pressure boundary condition as previous configurations. The simulation environment and pressure ranges are maintained from the previous geometry configurations.

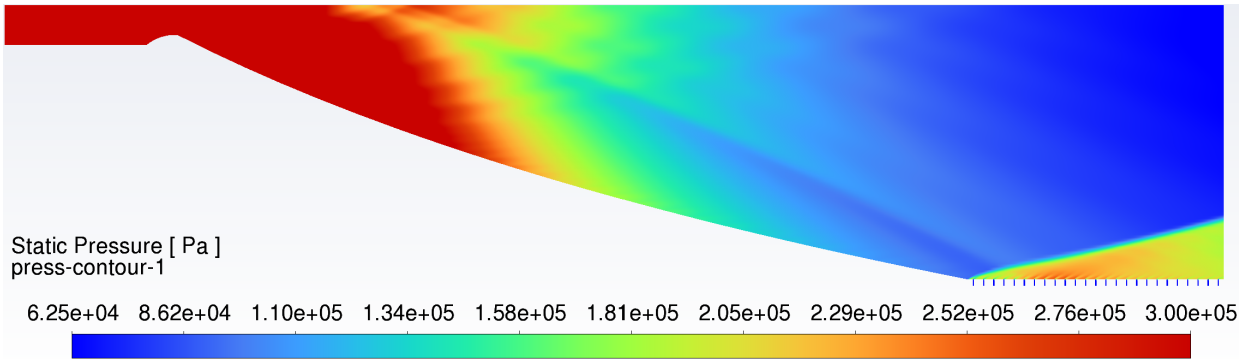


Fig. 5.7 Static pressure distribution of full 2D rocket geometry with porous bleed region at a 25 hole configuration of 5 mm diameter.

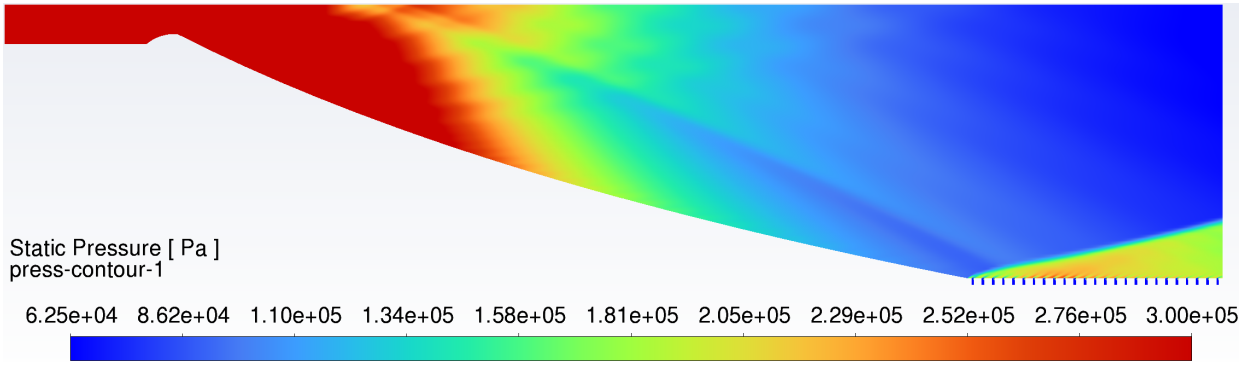


Fig. 5.8 Static pressure distribution of full 2D rocket geometry with porous bleed region at a 25 hole configuration of 10 mm diameter.

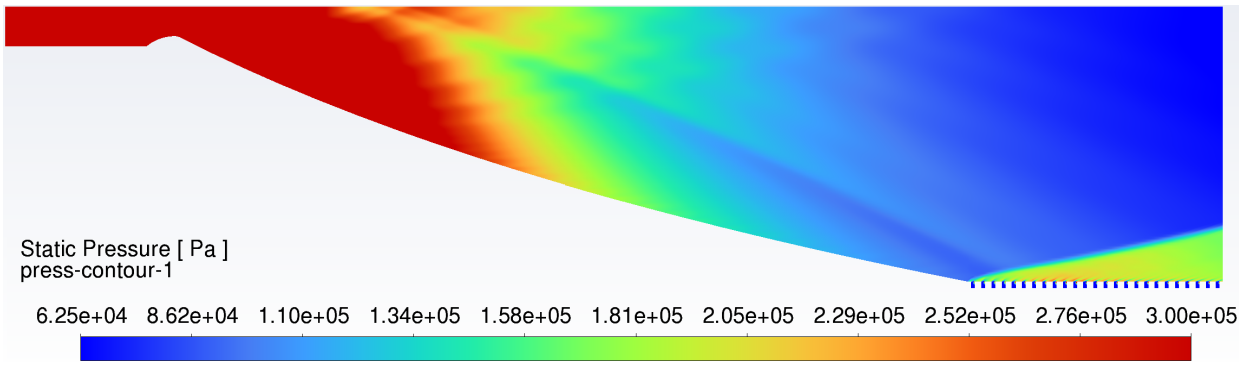


Fig. 5.9 Static pressure distribution of full 2D rocket geometry with porous bleed region at a 25 hole configuration of 15 mm diameter.

From the static pressure contours collected, the porous region appears visually to demonstrate the same pressure reduction when compared to the non-porous compression corner geometry, but varies somewhat linearly in relative pressure reduction from largest hole diameter to smallest hole diameter. Even so, the predictive behavior resulting from the large pressure differential between the high pressure over the bleed section and the low pressure environment demonstrated boundary-layer suction through bleed passage [21].

In *Parameter Influence on Porous Bleed Performance for Shock-Wave/Boundary-Layer Interaction Control*, Giehler found that at very small bleed hole diameters of D $\leq$ 1 mm did not result in flow penetration through hole passages, but at D $\geq$ 1 mm penetration was observed. Additionally, shockwaves are generated at each hole by an expansion fan and barrier shock [22]. The shockwaves in their study are curved upward and decrease in homogeneity as diameter increases. In Fig. 5.16 a similar flow behavior is shown; where expansion fans produced by bleed holes form in the high pressure p_2 region.

5.2 Flow Simulation of Symmetric 3D Geometry

The three-dimensional CFD simulation is used to further investigate the impact of porosity in the rocket engine nozzle where shockwave behavior and flow characteristics become more complex when allowed to interact laterally. For example, localized zones of high pressure differentials around geometric edges are observed near the nozzle wall for the three-dimensional geometry where in the two-dimensional geometries they were not observable.

From Fig. 5.12 we can see the static pressure distribution along the wall through the length of the rocket engine. Interestingly, the pressure range that captures the clearest differential for the three-dimensional simulation is an order of magnitude less than that of the two-dimensional simulations in both upper and lower limits: 30 kPa and 8 kPa, respectively, for the same given initial and environmental conditions. This decrease in total pressure range appears to be unique to the three-dimensional nature of the internal environment and may be result of an inferior mesh resolution upstream, impacting metrics downstream.

Similar to the two-dimensional case, we see bleed hole penetration and longitudinal pressure gradients around hole edges. The static pressure also remains relatively constant in the radial dimension within the post-shock region, but diverges non-homogeneously when rotating about the circumference of fixed radii.

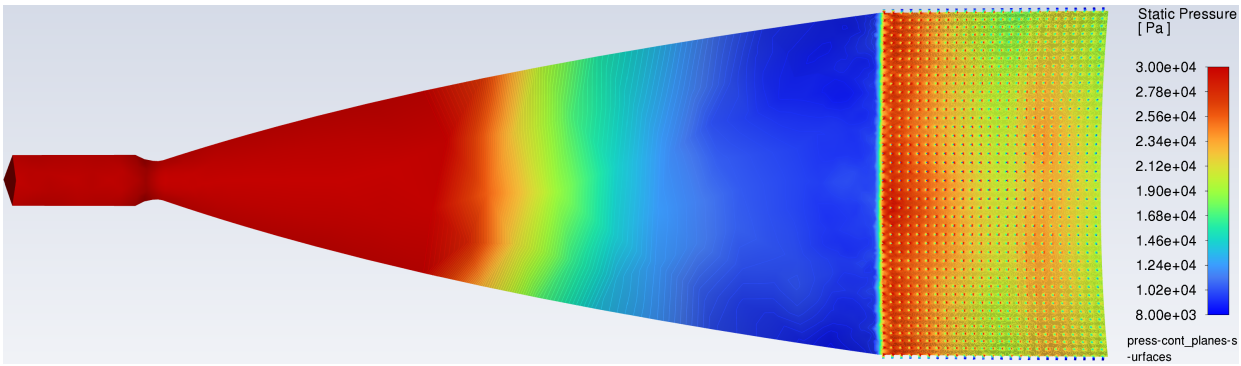
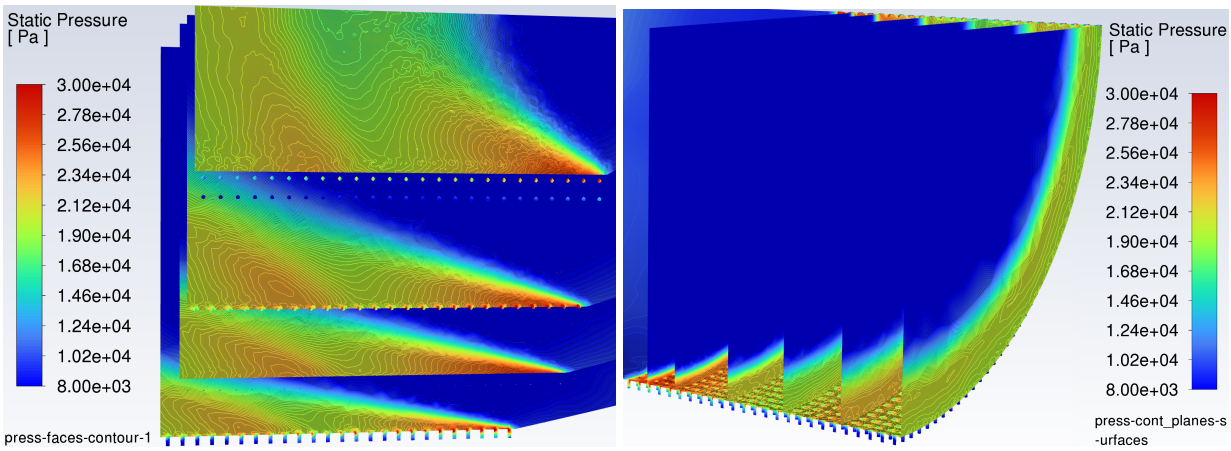


Fig. 5.10 Static pressure distribution along full-length rocket nozzle wall.

The concave compression corner generates a three-dimensional oblique shock that propagates radially inward as it travels downstream, forming an inverted conical shock surface. Unlike the planar shock structures characteristic of the two-dimensional compression ramps [23], the axisymmetric nozzle geometry allows the shock to expand circumstantially toward the centerline, causing the high-pressure region enclosed by the shock to increase in cross-sectional area with downstream distance. As a result, an increasingly larger fraction of the nozzle flow is subjected to compression, producing pressure gradients in both the streamwise and radial directions. This expanding shock footprint has important implications for wall pressure loading, shock-induced boundary-layer separation, and the interaction between the shock and downstream porous bleed regions, emphasizing the inherently three-dimensional nature of the flow.

It is observed that the shockwave boundary between the p_1 and p_2 regions becomes less uniform when compared to that of the two-dimensional geometry. This may be a function of simulation parameters such as mesh quality, where resolution diminished more drastically. Additionally, as a result of the radial geometry the resulting shockwave forms a converging conical wavefront where pressure transitions less asymptotically as flow travels downstream.



(a) Radially outward shockwave propagation interaction.

(b) Compression Corner 3D shockwave propagation along central axis.

Fig. 5.11 Static pressure contour of porous bleed region with 25 bleed holes with a 15 mm diameter.

One interesting consequence of the axisymmetric geometry is that the pressure rise produced by the concave compression corner is not experienced simultaneously throughout the nozzle cross-section. The boundary-layer adjacent to the nozzle wall encounters the oblique shock immediately after the compression corner, producing a localized increase in static pressure and the onset of an adverse pressure gradient. The pressure field develops progressively from the wall toward the core flow rather than uniformly across the nozzle.

As mentioned earlier, the compressed region enclosed by the shock occupies an increasingly larger fraction of the nozzle cross section with downstream distance, exposing a greater portion of the core flow to elevated static pressure while simultaneously broadening the region influenced by the adverse pressure gradient. This gradual inward propagation of the pressure field has important implications for the downstream flow development, influencing the size and shape of the shock-induced separation region, the redistribution of momentum within the nozzle, and the effectiveness

of passive flow-control techniques such as porous bleed, whose interaction with the shock evolves as the shock footprint expands downstream.

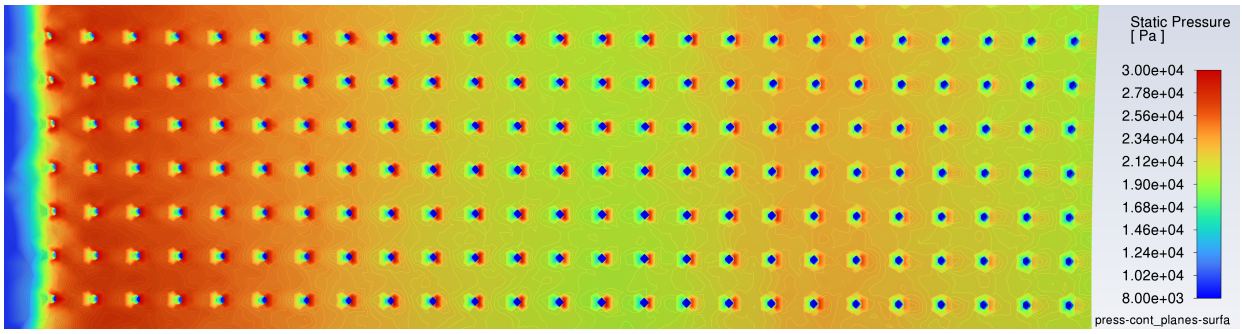


Fig. 5.12 Static pressure distribution at porous region wall with hole-gap interaction.

When observing Fig. 5.12 the wall-pressure distribution exhibits a sharp increase immediately downstream of the concave compression corner, corresponding to the initial compression imposed on the supersonic flow. Since the downstream porous section maintains a constant nozzle radius, the subsequent reduction in background wall pressure cannot be attributed to geometric area expansion. Rather, it may indicate the downstream adjustment of the compressed flow and the cumulative influence of boundary-layer extraction through the bleed array geometry.

Superimposed on the wall pressure field are strongly localized disturbances generated by each individual bleed hole. The low pressure regions centered at the hole openings are consistent with acceleration of near-wall fluid into the bleed passages under the imposed pressure differential. Adjacent high-pressure regions, most prominently located near the downstream edges of the openings, indicate local compression of the flow as it encounters the hole geometry and the suction-induced disturbance [24]. Farther downstream, the pressure disturbances produced by successive holes appear to broaden and overlap, indicating interaction among neighboring bleed elements.

The cumulative removal of low-momentum boundary-layer fluid modifies the near-wall momentum distribution and may contribute to the gradual streamwise evolution of the background pressure field within the bleed region. Overall, the contour illustrates the simultaneous presence of a global shock-induced pressure response and a superimposed network of localized bleed hole interactions, producing a complex three-dimensional wall-pressure distribution whose development is governed by shock propagation, boundary-layer adjustment, and discrete suction effects.

5.3 Numerical Results and Performance Trends

The two metrics of performance are specific to oblique shockwave presence and highlight preliminary assumptions based on trends from porosity area in hole diameter and discrete hole frequency. For each case where the overall porous bleed area within the p_2 region is increased a similar trend of relative average pressure drop and shockwave displacement distance decrease is observed.

With this, Table 5.2 highlights the numerical findings of the compression corner geometry shown in Fig. 5.3 and of the following porous region permutation contours.

Table 5.2 Performance Metric Results of Geometry Permutation at Nozzle Outlet

Geometry Permutation	**Displacement Distance, δ^* [mm]**	**Pressure Ratio, p_2/p_1**
No Porosity	245.3350	2.7135
4 Holes	227.1745	2.5583
8 Holes	210.5665	2.4102
12 Holes	196.9965	2.3213
5 mm Diameter Holes	240.4075	2.4592
10 mm Diameter Holes	226.9565	2.3569
15 mm Diameter Holes	211.5940	2.2594

A check can be made when observing results of each case with regards to overall static pressure as a function of radial wall distance. Referencing Fig.5.13 and Fig. 5.14 the static pressure, p_1, for all geometry configurations are in approximate agreement and reinforce the findings of variation in the p_2 region. (The pre-shock region is approximately $y \geq$ 210 mm and the post-shock region is approximately $y \leq$ 240 mm.)

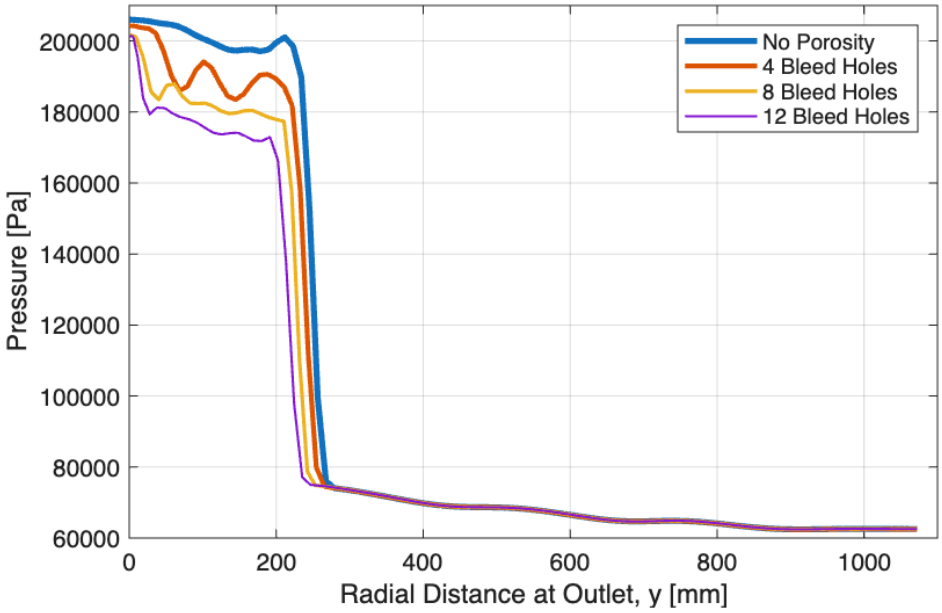


Fig. 5.13 Static Outlet Pressure Distribution with Variable Bleed Hole Number.

Notably, when varying the bleed hole number there appears to be greater amplitude in pressure rise and fall within the p_2 region, most dramatically in the 4-hole configuration. When looking at this region specifically for the varying hole number scenario, the pressure amplitude seems to decrease as the number increases (red line greatest:purple line least). To further this observation, in the varying bleed hole diameter scenario, and keeping the number of holes constant at 25, the pressure amplitude in the p_2 region fluctuates far less than that of the former scenario. Although, unique to the p_2 region for the diameter variation scenario appears to place pressure fluctuations at roughly the same radial distance between diameter variation geometries. This behavior highlights the impact each hole and hole distribution has on the entire post-shock region with regards to flow turbulence and pressure gradients.

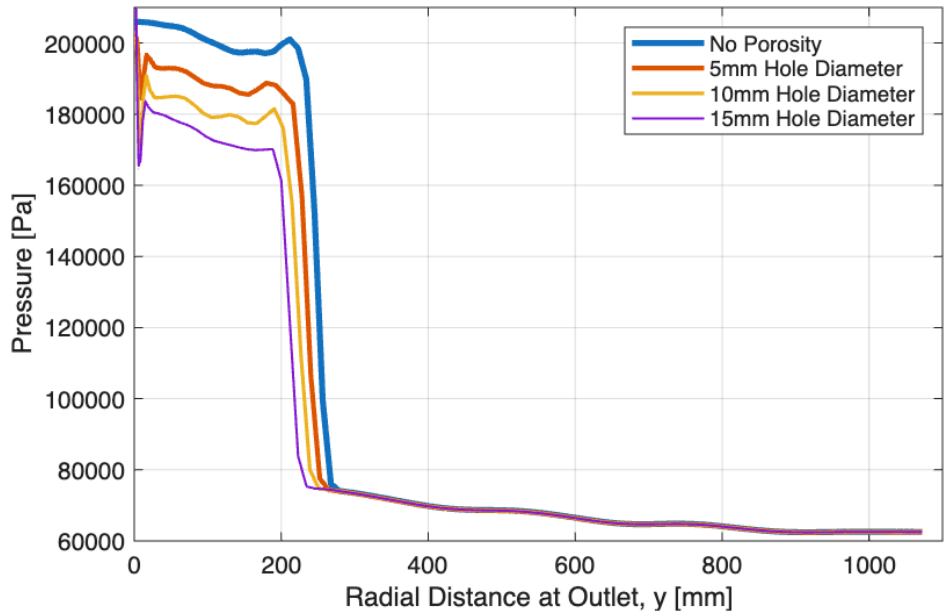
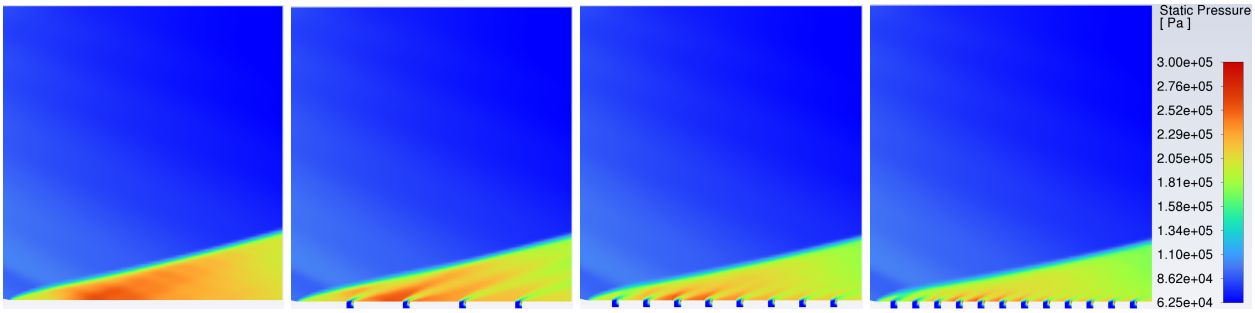
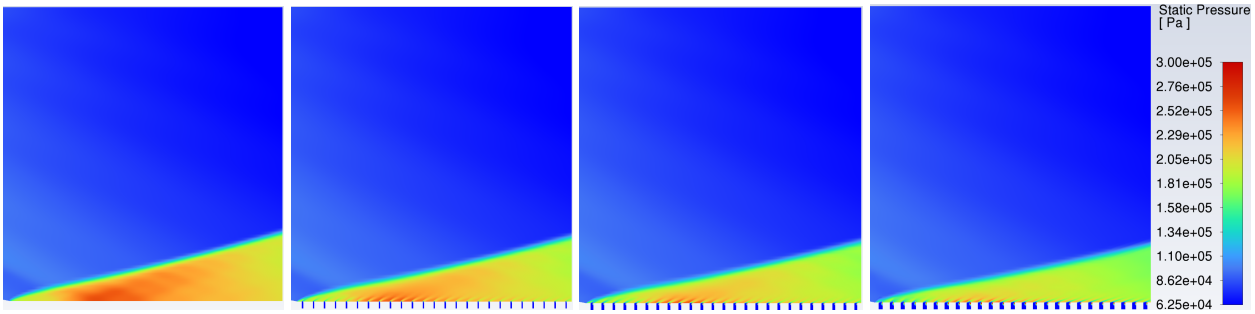


Fig. 5.14 Static Outlet Pressure Distribution with Variable Bleed Hole Diameter.



(a) No porosity. (b) 4-hole geometry. (c) 8-hole geometry. (d) 12-hole geometry.

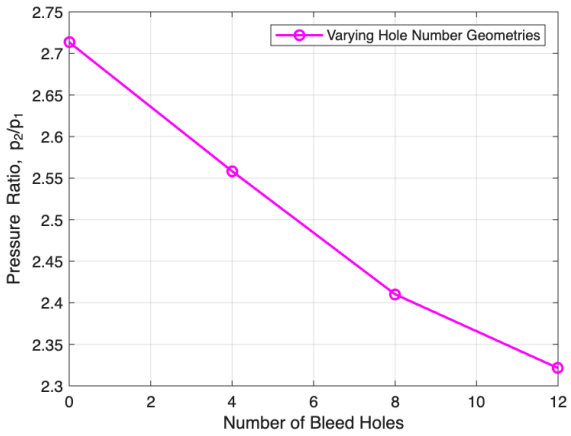
Fig. 5.15 Shock profile comparison of static pressure for the variable hole quantity geometries.



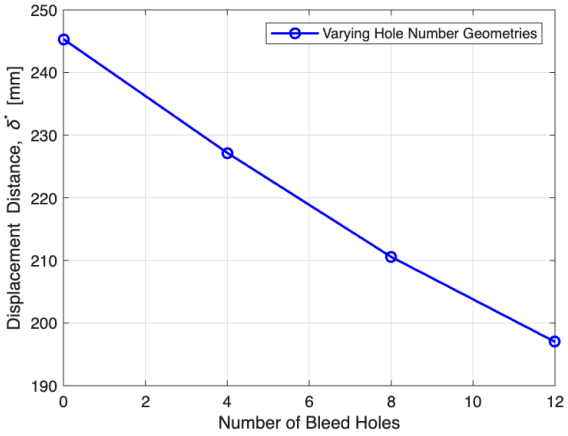
(a) No porosity. (b) 5 mm diameter (c) 10 mm diameter (d) 15 mm diameter

Fig. 5.16 Shock profile comparison of static pressure for the variable hole diameter geometries.

The resulting metrics demonstrate that both increasing the number of bleed holes and increasing the bleed hole diameter reduce the pressure rise and displacement distance measured at the nozzle outlet. For the nonporous baseline geometry, the displacement distance was 245.3350 mm, while the pressure ratio was p_2/p_1 = 2.7135. Introducing porosity produced a reduction in both quantities, indicating that boundary-layer bleed alters the downstream shock structure and decreases the extent of the compressed region. The static pressure contours support this observation: as porosity is increased, the high-pressure region downstream of the compression corner becomes progressively less intense, while the oblique shock front remains present. Thus, the bleed does not eliminate the compression wave within the tested range, but it weakens its downstream pressure signature and limits its displacement into the flow field.



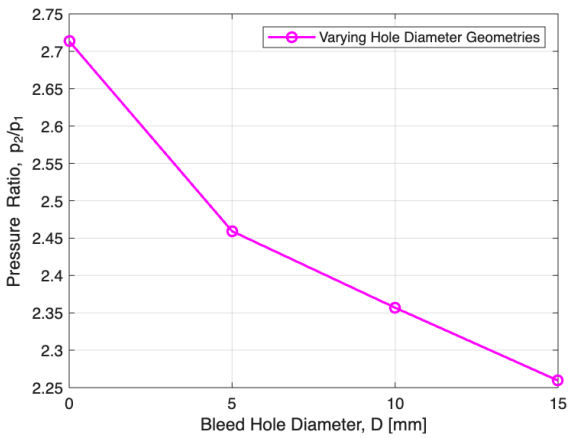
(a) Pressure ratio as a function of bleed hole number.



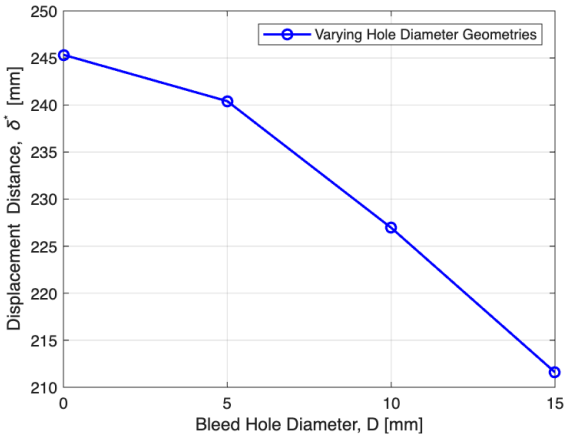
(b) Displacement distance as a function of bleed hole number.

Fig. 5.17 Variation in bleed hole number geometry configurations; trends in pressure ratio and displacement distance.

For the variable hole number geometries, increasing the number of holes from 4 to 12 produced a nearly continuous reduction in displacement distance. The 4-hole configuration reduced δ^* from 245.3350 mm to 227.1745 mm, while the 8- and 12-hole configurations reduced it further to 210.5665 mm and 196.9965 mm, respectively. Relative to the nonporous geometry, the 12-hole configuration produced a displacement reduction of approximately 19.7%. The pressure ratio followed the same general trend, decreasing from 2.7135 without porosity to 2.5583, 2.4102, and 2.3213 for the 4-, 8-, and 12-hole geometries. This corresponds to a maximum pressure ratio reduction of approximately 14.5%. The reduction between the 8- and 12-hole cases was smaller than that observed over the preceding intervals, suggesting that the benefit of adding additional holes may begin to diminish as a larger portion of the interaction region is already influenced by bleed.



(a) Pressure ratio as a function of bleed hole diameter.



(b) Displacement distance as a function of bleed hole diameter.

Fig. 5.18 Variation in bleed hole diameter geometry configurations; trends in pressure ratio and displacement distance.

Increasing the bleed hole diameter also improved both performance metrics, although the trends differed somewhat from those obtained by varying hole quantity. The 5 mm diameter geometry produced only a modest reduction in displacement distance, from 245.3350 mm to 240.4075 mm, but reduced the pressure ratio more substantially to 2.4592. Increasing the diameter to 10 and 15 mm lowered the displacement distance to 226.9565 mm and 211.5940 mm, respectively. The corresponding pressure ratios were 2.3569 and 2.2594. Therefore, the 15 mm configuration reduced the displacement distance by approximately 13.8% and the pressure ratio by approximately 16.7% relative to the nonporous case. This behavior is consistent with the greater open area and potential bleed capacity provided by larger holes [22], which allow a greater portion of the near-wall flow to be extracted and produce a stronger modification of the shock–boundary-layer interaction.

A comparison of the two parameter studies indicates that hole number and hole diameter affect the flow in different ways. The 12-hole geometry produced the smallest displacement distance of all tested cases, whereas the 15 mm diameter geometry produced the lowest pressure ratio. Increasing the number of holes may provide a more distributed bleed effect over the interaction region, thereby limiting the spatial development of the shock-affected flow. In contrast, increasing hole diameter may produce stronger localized extraction and a greater decrease in the pressure rise. Consequently, no single configuration is superior according to both metrics: the preferred geometry depends on whether minimizing shock displacement or minimizing the outlet pressure ratio is considered the primary design objective.

6 Conclusion

This study computationally evaluated the feasibility of using downstream porous bleed to modify the shock–boundary-layer interaction generated by a concave compression corner within a supersonic rocket nozzle. A full-length converging-diverging nozzle was analyzed using the density-based, steady Reynolds-averaged Navier–Stokes formulation with the SST $k-\omega$ turbulence model under near-vacuum operating conditions. The control geometry reproduced the expected pressure and Mach-number behavior of a de Laval nozzle, while the introduction of an 11.1° compression corner generated a distinct oblique shock and an associated post-shock pressure rise. A nonporous compression-corner configuration provided the baseline against which two-dimensional porous geometries with varying hole quantity and diameter were assessed, followed by a three-dimensional quarter-sector simulation incorporating a circumferential array of discrete bleed holes.

The two-dimensional results demonstrated that increasing the available bleed area consistently reduced both the outlet pressure ratio and the displacement distance of the shock-affected region. The nonporous configuration produced a displacement distance of 245.3350 mm and a pressure ratio of $p_2/p_1 = 2.7135$. Increasing the number of 25 mm bleed holes from 4 to 12 reduced these quantities progressively, with the 12-hole configuration producing the smallest displacement distance of 196.9965 mm, corresponding to a reduction of approximately 19.7%, and a pressure-ratio reduction of approximately 14.5%. Increasing the diameter of the 25-hole configurations from 5 to 15 mm produced a similar improvement, with the 15 mm configuration yielding the lowest pressure ratio of 2.2594, a reduction of approximately 16.7%, and a displacement-distance reduction of approximately 13.8%. These results indicate that hole quantity and hole diameter affect the interaction differently: a greater number of holes distributes the bleed influence over a larger portion of the interaction region, whereas larger holes provide stronger localized extraction and a greater reduction in the post-shock pressure rise. Although none of the tested configurations eliminated the oblique shock, porous bleed measurably weakened its downstream pressure signature and reduced its penetration into the nozzle flow field.

The three-dimensional simulation further illustrated the complexity of implementing porous bleed in an axisymmetric nozzle. The compression corner generated an inward-propagating, conical shock surface whose footprint expanded through the nozzle cross-section with downstream distance. At the porous wall, each bleed hole produced a localized low-pressure region associated with acceleration into the passage, accompanied by adjacent compression regions and interactions between disturbances generated by neighboring holes. Collectively, the results support porous bleed as a potentially effective method for controlling localized internal shock structures in rocket nozzles, while also demonstrating that its performance depends on the distribution and scale of the bleed geometry. The present conclusions remain subject to the steady-RANS assumptions, computational iteration limits, and reduced three-dimensional mesh resolution imposed by the available software license. Future work should therefore include mesh- and turbulence-model-independence studies, transient simulations, direct evaluation of wall shear stress and separation, measurement of bleed mass flow and thrust penalties, optimization of hole spacing and porosity, and higher-fidelity treatment of the bleed exhaust where rarefaction may invalidate the continuum assumption.

References

[1] Anderson, J. D., *Fundamentals of Aerodynamics*, McGraw-Hill, 5th ed., 2011.

[2] Sriram, R. and Jagadeesh, G., "Shock tunnel experiments on control of shock induced large separation bubble using boundary layer bleed," *Aerospace Science and Technology*, Vol. 36, 2014, pp. 87–93.

[3] Missing, T., Bulut, J., Schrijer, F., van Oudheusden, B., and Babinsky, H., "Separation bubble shaped control bumps for turbulent oblique shock wave–boundary-layer interactions," *Journal of Fluid Mechanics*, Vol. 1028, 2026, pp. A2.

[4] Smits, A. J. and Dussauge, J.-P., *Turbulent Shear Layers in Supersonic Flow*, Springer, 2nd ed., 2006.

[5] Souverein, L., Dupont, P., Dussauge, J.-P., Oudheusden, B., and Scarano, F., "Effect of Interaction Strength on Unsteadiness in Shock-Wave-Induced Separations," *AIAA*, Vol. 48, 07 2010, pp. 1480–1493.

[6] Zebiri, B., Piquet, A., Hadjadj, A., and Verma, S. B., "Shock-Induced Flow Separation in an Overexpanded Supersonic Planar Nozzle," *AIAA Journal*, Vol. 58, No. 5, 2020, pp. 2122–2131.

[7] Stark, R. and Genin, C., "Flow Separation in Rocket Nozzles Under High Altitude Condition," *Shock Waves*, Vol. 27, 2017, pp. 63–68.

[8] Hu, H., G. X. G. Y. . Y. J., "Shock Wave and Aeroelastic Coupling in Overexpanded Nozzle," *Aerospace*, Vol. 11, No. 10, 2024.

[9] Giehler, J., Leudiere, T., Morgadinho, R. S., Grenson, P., and Bur, R., "Experimental and numerical investigation of porous bleed control for supersonic/subsonic flows, and shock-wave/boundary-layer interactions," *Aerospace Science and Technology*, Vol. 147, 2024, pp. 109062.

[10] Zuo, F.-Y., Ma, L.-J., Wang, S.-Q., and Pirozzoli, S., "Suppression separation in conical shock wave/turbulent boundary layer interactions through porous bleed control," *Propulsion and Power Research*, Vol. 15, No. 1, 2026, pp. 1–15.

[11] Slater, J., "Improvements in Modeling 90° Bleed Holes for Supersonic Inlets," *AIAA*, Vol. 2009, No. 0710, 2009.

[12] Morell, A. T., *Model for Flow Properties Across the Opening of Normal Bleed Holes*, Master's thesis, University of Cincinnati, 2017.

[13] LeBeau, G. and Lumpkin III, F., "Application highlights of the DSMC Analysis Code (DAC) software for simulating rarefied flows," *Computer Methods in Applied Mechanics and Engineering*, Vol. 191, No. 6, 2001, pp. 595–609, Minisymposium on Methods for Flow Simulation and Modeling.

[14] B. D. Stewart, F. E. Lumpkin, and G. J. LeBeau, "Axisymmetric Implimentation for 3D-Based DSMC Codes," https://ntrs.nasa.gov/api/citations/20110015744/downloads/20110015744.pdf, 2011, [Online; accessed 5-February-2026].

[15] Wevolver, "Merlin Engine (Merlin-1D) - Falcon 9 & Falcon Heavy," https://www.wevolver.com/specs/merlin-engine-merlin-1d-falcon-9-falcon-heavy, n.d., Retrieved May 11, 2026.

[16] Huzel, D. K., Huang, D. H., and Arbit, H., *Modern Engineering for Design of Liquid-propellant Rocket Engines*, Progress in astronautics and aeronautics, v. 147, American Institute of Aeronautics and Astronautics, Washington, D.C, revised, updated, and enlarged / by harry arbit [and others]. ed., 1992.

[17] Hamaidia, W., Yahiaoui, T., and Sellam, M., "CFD investigation of supersonic two parallel expansions nozzles," *Advances in Space Research*, Vol. 75, No. 2, 2025, pp. 2378–2390.

[18] Yang, K., Lee, J., Lee, S., Kim, H., Sheen, D., and Park, C., "Numerical Simulation Of Supersonic Compression Ramp Flow," *Turkish Journal of Computer and Mathematics Education*, Vol. 12, No. 6, 2021, pp. 812–822.

[19] ANSYS, Inc., "CFD Meshing Strategy," ANSYS Help, https://ansyshelp.ansys.com/public/account/secured?returnurl=/Views/Secured/corp/v261/en/wb_msh/msh_cfd_strategy.html, 2026, Accessed: July 31, 2026.

[20] Edwards, J. R., "Numerical simulations of shock/boundary layer interactions using time-dependent modeling techniques: A survey of recent results," *Progress in Aerospace Sciences*, Vol. 44, No. 6, 2008, pp. 447–465, Large Eddy Simulation - Current Capabilities and Areas of Needed Research.

[21] Kim, S. D., "A computational study on the influence of a bleed slot on the flowfield of a bump-type inlet," *Journal of Mechanical Science and Technology*, Vol. 29, No. 12, 12 2015, pp. 5245–5250.

[22] Giehler, J., Grenson, P., and Bur, R., *Parameter Influence on Porous Bleed Performance for Shock-Wave/Boundary-Layer Interaction Control*, Springer Nature Switzerland, Cham, 2025, pp. 127–147.

[23] Park, Y., Nam, J., Lee, B. J., and Lee, Y. J., "Experimental and numerical investigation of the effects of porous bleed systems on a model scramjet inlet under high backpressure conditions," *Aerospace Science and Technology*, Vol. 151, 2024, pp. 109264.

[24] Wang, C., Eri, Q., Kong, B., Wang, Y., and Ding, W., "Novel Simplified Numerical Simulation Method for Modeling Bleed Holes in Supersonic Inlets," *AIAA Journal*, Vol. 60, No. 12, 2022, pp. 6926–6939.

Appendix A
Control Configuration Engineering Drawing

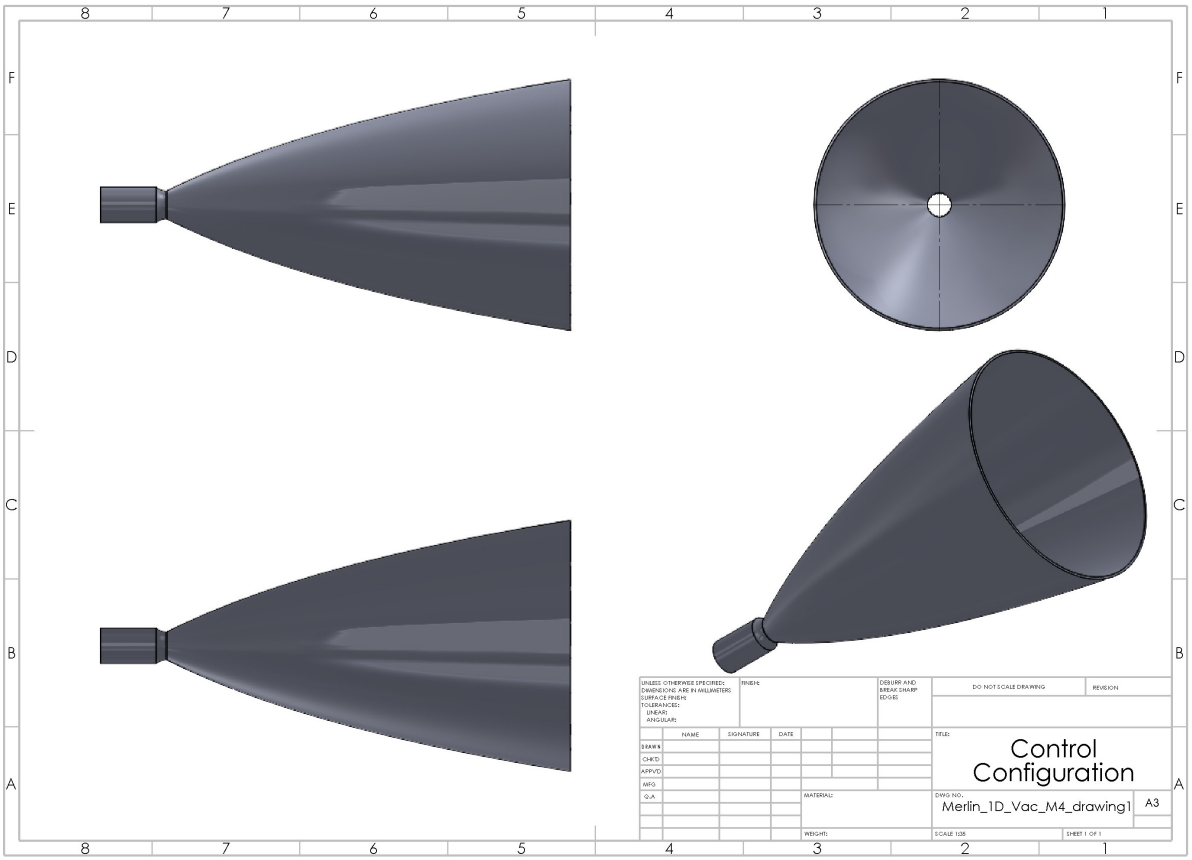


Fig. A.1 Engineering drawing of 3D rocket engine control configuration in SolidWorks.

Appendix B
ANSYS Fluent Residuals Charts

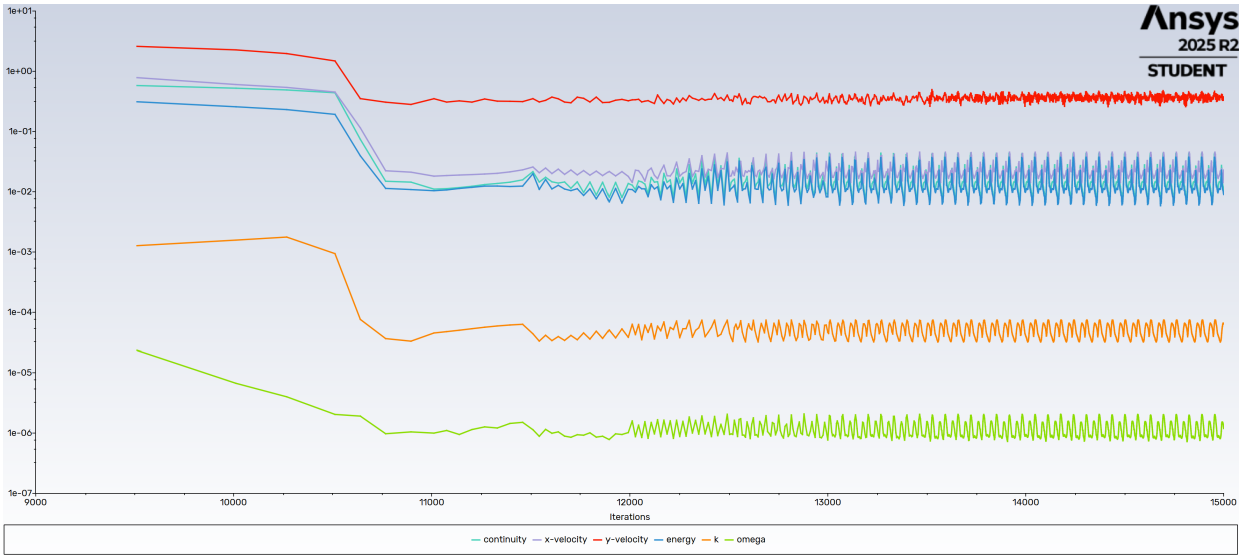


Fig. B.1 Example simulation residuals result for the variable hole diameter 2D symmetric geometry.

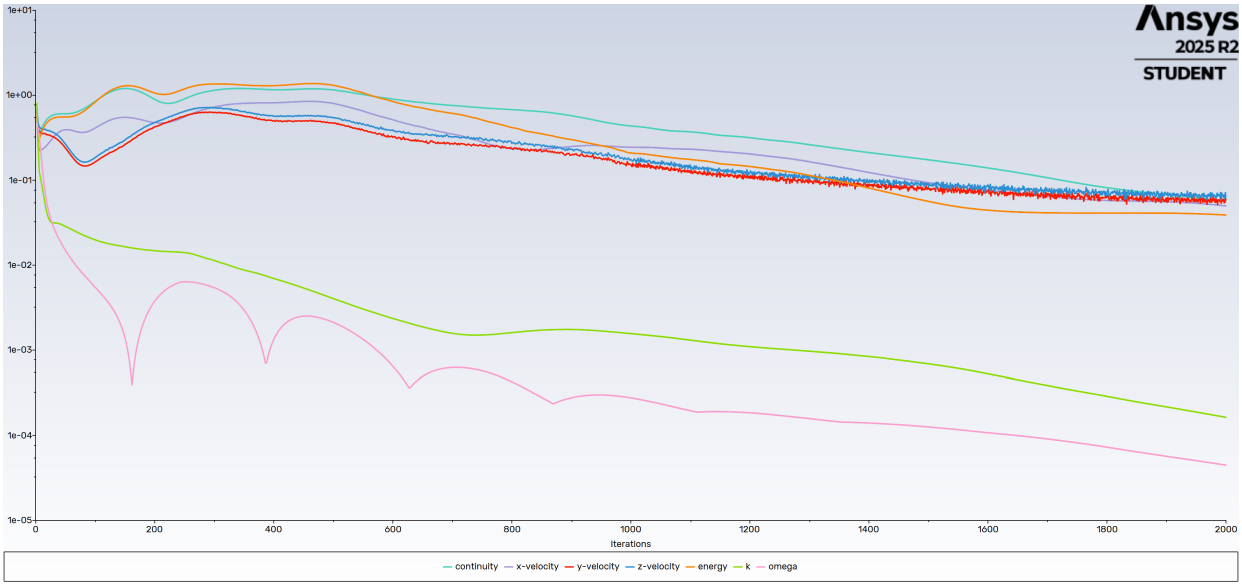


Fig. B.2 Example simulation residuals result for the 3D axisymmetric quarter-volume geometry.

Appendix C
MATLAB Script: Outlet Data Analysis for Varying Hole Quantity Configurations

```
%% Analysis of Outlet Data of Vh4-2 Geometry, Constant Diameter Case
% By: Mathias Guillen

%% Import Data

clear; clc;

% CORNER (0) Geometry Data
stat_press_outlet_raw_0 = 'stat_press_outlet_data_Corner0';
data_0 = readmatrix(stat_press_outlet_raw_0, ...
                    'FileType', 'text', ...
                    'Delimiter', ',', ...
                    'NumHeaderLines', 1);
node_num0 = data_0(:,1);
x0_coord_m = data_0(:,2);
y0_coord_m = data_0(:,3);
stat_press0 = data_0(:,5);

% POROUS_4 (1) Geometry Data
stat_press_outlet_raw_1 = 'stat_press_outlet_data_Porous1';
data_1 = readmatrix(stat_press_outlet_raw_1, ...
                    'FileType', 'text', ...
                    'Delimiter', ',', ...
                    'NumHeaderLines', 1);
node_num1 = data_1(:,1);
x1_coord_m = data_1(:,2);
y1_coord_m = data_1(:,3);
stat_press1 = data_1(:,6);

% POROUS_8 (2) Geometry Data
stat_press_outlet_raw_2 = 'stat_press_outlet_data_Porous2';
data_2 = readmatrix(stat_press_outlet_raw_2, ...
                    'FileType', 'text', ...
                    'Delimiter', ',', ...
                    'NumHeaderLines', 1);
node_num2 = data_2(:,1);
x2_coord_m = data_2(:,2);
y2_coord_m = data_2(:,3);
stat_press2 = data_2(:,6);

% POROUS_12 (3) Geometry Data
stat_press_outlet_raw_3 = 'stat_press_outlet_data_Porous3';
data_3 = readmatrix(stat_press_outlet_raw_3, ...
                    'FileType', 'text', ...
                    'Delimiter', ',', ...
                    'NumHeaderLines', 1);
node_num3 = data_3(:,1);
x3_coord_m = data_3(:,2);
y3_coord_m = data_3(:,3);
```

```
stat_press3 = data_3(:,6);

% display(y1_coord_m)

%% Parsing and Adjusting Data
clc;

% Converting Coords from meters to millimeters
x0_coord_mm = x0_coord_m * 1000;
y0_coord_mm = y0_coord_m * 1000;

x1_coord_mm = x1_coord_m * 1000;
y1_coord_mm = y1_coord_m * 1000;

x2_coord_mm = x2_coord_m * 1000;
y2_coord_mm = y2_coord_m * 1000;

x3_coord_mm = x3_coord_m * 1000;
y3_coord_mm = y3_coord_m * 1000;

% Set y-coords 0 at Wall
y0_coord_mm_reodered = y0_coord_mm - min(y0_coord_mm);
y1_coord_mm_reodered = y1_coord_mm - min(y1_coord_mm);
y2_coord_mm_reodered = y2_coord_mm - min(y2_coord_mm);
y3_coord_mm_reodered = y3_coord_mm - min(y3_coord_mm);

%% Initial Plots for Inspection

% CORNER (0) Initial Plot
figure;
    plot(y0_coord_mm_reodered, stat_press0, 'LineWidth', 1.5);
    grid on;
    ax = gca;
    ax.XAxis.Exponent = 0;
    ax.YAxis.Exponent = 0;
    xlim([0 1100]);
    ylim([60000 210000]);
    xlabel('Y-Coordinate [mm]');
    ylabel('Static Pressure [Pa]');
    title('Static Pressure Distribution at Outlet, Corner Geomtry');

% POROUS_4 (1) Initial Plot
figure;
    plot(y1_coord_mm_reodered, stat_press1, 'LineWidth', 1.5);
    grid on;
    ax = gca;
    ax.XAxis.Exponent = 0;
    ax.YAxis.Exponent = 0;
    xlim([0 1100]);
    ylim([60000 210000]);
    xlabel('Y-Coordinate [mm]');
    ylabel('Static Pressure [Pa]');
    title('Static Pressure Distribution at Outlet, Porous 4 Geometry');

```

```
% POROUS_8 (2) Initial Plot
figure;
    plot(y2_coord_mm_reodered, stat_press2, 'LineWidth', 1.5);
    grid on;
    ax = gca;
    ax.XAxis.Exponent = 0;
    ax.YAxis.Exponent = 0;
    xlim([0 1100]);
    ylim([60000 210000]);
    xlabel('Y-Coordinate [mm]');
    ylabel('Static Pressure [Pa]');
    title('Static Pressure Distribution at Outlet, Porous 8 Geometry');

% POROUS_12 (3) Initial Plot
figure;
    plot(y3_coord_mm_reodered, stat_press3, 'LineWidth', 1.5);
    grid on;
    ax = gca;
    ax.XAxis.Exponent = 0;
    ax.YAxis.Exponent = 0;
    xlim([0 1100]);
    ylim([60000 210000]);
    xlabel('Y-Coordinate [mm]');
    ylabel('Static Pressure [Pa]');
    title('Static Pressure Distribution at Outlet, Porous 12 Geometry');

%% Pressure Ratio Calculations
clc;

% Pressure Ratios Immediatly Before and After Shockwave
% CORNER (0)
p1_0 = 74090.9; % Pa
y1_0 = 278.87; % mm
p2_0 = 201045; % Pa
y2_0 = 211.8; % mm
p2_p1_0 = p2_0 / p1_0; % Ratio

% POROUS_4 (1)
p1_1 = 74508.9; % Pa
y1_1 = 265.549; % mm
p2_1 = 190615; % Pa
y2_1 = 188.8; % mm
p2_p1_1 = p2_1 / p1_1; % Ratio

% POROUS_8 (2)
p1_2 = 74856; % Pa
y1_2 = 253.141; % mm
p2_2 = 180418; % Pa
y2_2 = 167.992; % mm
p2_p1_2 = p2_2 / p1_2; % Ratio

% POROUS_12 (3)
p1_3 = 75026.4; % Pa
y1_3 = 246.345; % mm
```

```
p2_3 = 174162; % Pa
y2_3 = 147.648; % mm
p2_p1_3 = p2_3 / p1_3; % Ratio

fprintf('CORNER Pressure Ratio, p2/p1 = %.4f\n', p2_p1_0);
fprintf('POROUS_4 Pressure Ratio, p2/p1 = %.4f\n', p2_p1_1);
fprintf('POROUS_8 Pressure Ratio, p2/p1 = %.4f\n', p2_p1_2);
fprintf('POROUS_12 Pressure Ratio, p2/p1 = %.4f\n\n', p2_p1_3);

%% Displacement Distance Calculations (shockwave height at Outlet)
% clc;

% CORNER (0)
d_star_0 = ((y1_0 - y2_0) / 2) + y2_0; % mm
% POROUS_4 (1)
d_star_1 = ((y1_1 - y2_1) / 2) + y2_1; % mm
% POROUS_8 (2)
d_star_2 = ((y1_2 - y2_2) / 2) + y2_2; % mm
% POROUS_12 (3)
d_star_3 = ((y1_3 - y2_3) / 2) + y2_3; % mm

fprintf('CORNER Displacement Distance = %.4f mm\n', d_star_0);
fprintf('POROUS_4 Displacement Distance = %.4f mm\n', d_star_1);
fprintf('POROUS_8 Displacement Distance = %.4f mm\n', d_star_2);
fprintf('POROUS_12 Displacement Distance = %.4f mm\n', d_star_3);

%% Creating Arrays of Combined Results

% Number of Bleed Holes for each geometry
numBleedHoles1 = [0, 4, 8, 12];

% Pressure Ratio for each geometry
p_ratios_array1 = [p2_p1_0, p2_p1_1, p2_p1_2, p2_p1_3];

% Displacement Distance for each geometry
disp_array1 = [d_star_0, d_star_1, d_star_2, d_star_3];

%% Individual Plots of Static Pressure Distribution for Each Geomety

% CORNER (0)
figure;
    plot(y0_coord_mm_reodered, stat_press0, 'LineWidth', 1.5);
    hold on;
    xline(y2_0, '--');
    xline(y1_0, '-');
    grid on;
    ax = gca;
    ax.XAxis.Exponent = 0;
    ax.YAxis.Exponent = 0;
    xlim([0 1100]);
    ylim([60000 210000]);
    xlabel('Y-coordinate [mm]')
    ylabel('Pressure [Pa]');
    title('Static Pressure Distribution at Outlet, Corner Geometry');
```

```
    legend('Outlet Pressure', 'p2 region Post-shock', 'p1 region Pre-shock');

% POROUS_4 (1)
    figure;
    plot(y1_coord_mm_reodered, stat_press1, 'LineWidth', 1.5);
    hold on;
    xline(y2_1, '--');
    xline(y1_1, '-');
    grid on;
    ax = gca;
    ax.XAxis.Exponent = 0;
    ax.YAxis.Exponent = 0;
    xlim([0 1100]);
    ylim([60000 210000]);
    xlabel('Y-coordinate [mm]')
    ylabel('Pressure [Pa]');
    title('Static Pressure Distribution at Outlet, Porous 4 Geometry');
    legend('Outlet Pressure', 'p2 region Post-shock', 'p1 region Pre-shock');

% POROUS_8 (2)
figure;
    plot(y2_coord_mm_reodered, stat_press2, 'LineWidth', 1.5);
    hold on;
    xline(y2_2, '--');
    xline(y1_2, '-');
    grid on;
    ax = gca;
    ax.XAxis.Exponent = 0;
    ax.YAxis.Exponent = 0;
    xlim([0 1100]);
    ylim([60000 210000]);
    xlabel('Y-coordinate [mm]')
    ylabel('Pressure [Pa]');
    title('Static Pressure Distribution at Outlet, Porous 8 Geometry');
    legend('Outlet Pressure', 'p2 region Post-shock', 'p1 region Pre-shock');

% POROUS_12 (3)
figure;
    plot(y3_coord_mm_reodered, stat_press3, 'LineWidth', 1.5);
    hold on;
    xline(y2_3, '--');
    xline(y1_3, '-');
    grid on;
    ax = gca;
    ax.XAxis.Exponent = 0;
    ax.YAxis.Exponent = 0;
    xlim([0 1100]);
    ylim([60000 210000]);
    xlabel('Y-coordinate [mm]')
    ylabel('Pressure [Pa]');
    title('Static Pressure Distribution at Outlet, Porous 12 Geometry');
    legend('Outlet Pressure', 'p2 region Post-shock', 'p1 region Pre-shock');

%% COMBINED Pressure Plots of Results
```

```
266
267 fig_width_comb1 = 6;
268 fig_height_comb1 = 3.75;
269
270 % Combined RANGED View of Static Pressure Distribution for Each Geomety
271 figure('Name','Combined Pressues-numBleedHoles','Units','inches','Position',...
272     [1, 1, fig_width_comb1, fig_height_comb1]);
273     plot(y0_coord_mm_reodered, stat_press0, 'LineWidth', 2.5);
274     hold on;
275     plot(y1_coord_mm_reodered, stat_press1, 'LineWidth', 2);
276     hold on;
277     plot(y2_coord_mm_reodered, stat_press2, 'LineWidth', 1.5);
278     hold on;
279     plot(y3_coord_mm_reodered, stat_press3, 'LineWidth', 1.0);
280     grid on;
281     ax = gca;
282     ax.XAxis.Exponent = 0;
283     ax.YAxis.Exponent = 0;
284     xlim([0 1100]);
285     ylim([60000 210000]);
286     xlabel('Radial Distance at Outlet, y [mm]')
287     ylabel('Pressure [Pa]');
288     % title('Static Outlet Pressure Distribution with Variable Bleed Hole Number');
289     legend('No Porosity', '4 Bleed Holes', '8 Bleed Holes', '12 Bleed Holes');
290
291 %% Data Trends Plots of Results
292 fig_width_trends1 = 5.5;
293 fig_height_trends1 = 4;
294
295 % Pressure Ratio as a Function of Bleed Hole Number
296 figure('Name','PressureRatio_Vs_numBleedHoles','Units','inches','Position',...
297     [1, 1, fig_width_trends1, fig_height_trends1]);
298     plot(numBleedHoles1, p_ratios_array1, '-om', 'LineWidth', 1.5);
299     hold on;
300     % scatter(numBleedHoles1, p_ratios_array1, 'LineWidth', 2.5);
301     grid on;
302     xlabel('Number of Bleed Holes')
303     % ylabel('^{p_2}/_{p_1}');
304     ylabel('Pressure Ratio, p_2/p_1');
305     % title('Pressure Ratio as a function of Bleed Hole Number');
306     legend('Varying Hole Number Geometries');
307
308 % Displacement Distance as a Function of Bleed Hole Number
309 figure('Name','DispDistance_Vs_numBleedHoles','Units','inches','Position',...
310     [1, 1, fig_width_trends1, fig_height_trends1]);
311     plot(numBleedHoles1, disp_array1, '-ob', 'LineWidth', 1.5);
312     hold on;
313     % scatter(numBleedHoles1, disp_array1, 'LineWidth', 2.5);
314     grid on;
315     xlabel('Number of Bleed Holes')
316     ylabel('Displacement Distance, \delta^* [mm]');
317     % title('Displacement Distance as a function of Bleed Hole Number');
318     legend('Varying Hole Number Geometries');
319
```

```
%% Data Trends Plots of Results - Side-by-Side
fig_width_trends2 = 13;
fig_height_trends2 = 5;

figure('Name','Trends_Plots-numBleedHoles','Units','inches','Position',...
    [1, 1, fig_width_trends2, fig_height_trends2]);
    subplot(1, 2, 1)
        plot(numBleedHoles1, p_ratios_array1, 'LineWidth', 1.5);
        hold on;
        scatter(numBleedHoles1, p_ratios_array1, 'LineWidth', 2.5);
        grid on;
        xlabel('Number of Bleed Holes')
        ylabel('Pressure Ratio, p_2/p_1');
        title('Pressure Ratio as a Function of Bleed Hole Number');
    subplot(1, 2, 2)
        plot(numBleedHoles1, disp_array1, 'LineWidth', 1.5);
        hold on;
        scatter(numBleedHoles1, disp_array1, 'LineWidth', 2.5);
        grid on;
        xlabel('Number of Bleed Holes')
        ylabel('Displacement Distance, \delta^* [mm]');
        title('Displacement Distance as a Function of Bleed Hole Number');
```

Appendix D
MATLAB Script: Outlet Data Analysis for Varying Hole Diameter Configurations

```
%% Analysis of Outlet Data of Vh4-2 Geometry, Constant Hole Number Case
% By: Mathias Guillen

%% Import Data

clear; clc;

% CORNER (0) Geometry Data
stat_press_outlet_raw_0 = 'stat_press_outlet_data_Corner0';
data_0 = readmatrix(stat_press_outlet_raw_0, ...
                    'FileType', 'text', ...
                    'Delimiter', ',', ...
                    'NumHeaderLines', 1);
node_num0 = data_0(:,1);
x0_coord_m = data_0(:,2);
y0_coord_m = data_0(:,3);
stat_press0 = data_0(:,5);

% POROUS_5mm (11) Geometry Data
stat_press_outlet_raw_11 = 'stat_press_outlet_data_Porous11';
data_11 = readmatrix(stat_press_outlet_raw_11, ...
                    'FileType', 'text', ...
                    'Delimiter', ',', ...
                    'NumHeaderLines', 1);
node_num11 = data_11(:,1);
x11_coord_m = data_11(:,2);
y11_coord_m = data_11(:,3);
stat_press11 = data_11(:,6);

% POROUS_10mm (22) Geometry Data
stat_press_outlet_raw_22 = 'stat_press_outlet_data_Porous22';
data_22 = readmatrix(stat_press_outlet_raw_22, ...
                    'FileType', 'text', ...
                    'Delimiter', ',', ...
                    'NumHeaderLines', 1);
node_num22 = data_22(:,1);
x22_coord_m = data_22(:,2);
y22_coord_m = data_22(:,3);
stat_press22 = data_22(:,6);

% POROUS_15mm (33) Geometry Data
stat_press_outlet_raw_33 = 'stat_press_outlet_data_Porous33';
data_33 = readmatrix(stat_press_outlet_raw_33, ...
                    'FileType', 'text', ...
                    'Delimiter', ',', ...
                    'NumHeaderLines', 1);
node_num33 = data_33(:,1);
x33_coord_m = data_33(:,2);
y33_coord_m = data_33(:,3);
```

```
stat_press33 = data_33(:,6);

% display(y11_coord_m)

%% Parsing and Adjusting Data
clc;

% Converting Coords from meters to millimeters
x0_coord_mm = x0_coord_m * 1000;
y0_coord_mm = y0_coord_m * 1000;

x11_coord_mm = x11_coord_m * 1000;
y11_coord_mm = y11_coord_m * 1000;

x22_coord_mm = x22_coord_m * 1000;
y22_coord_mm = y22_coord_m * 1000;

x33_coord_mm = x33_coord_m * 1000;
y33_coord_mm = y33_coord_m * 1000;

% Set y-coords 0 at Wall
y0_coord_mm_reodered = y0_coord_mm - min(y0_coord_mm);
y11_coord_mm_reodered = y11_coord_mm - min(y11_coord_mm);
y22_coord_mm_reodered = y22_coord_mm - min(y22_coord_mm);
y33_coord_mm_reodered = y33_coord_mm - min(y33_coord_mm);

%% Initial Plots for Inspection

% CORNER (0) Initial Plot
figure;
    plot(y0_coord_mm_reodered, stat_press0, 'LineWidth', 1.5);
    grid on;
    ax = gca;
    ax.XAxis.Exponent = 0;
    ax.YAxis.Exponent = 0;
    xlim([0 1100]);
    ylim([60000 210000]);
    xlabel('Y-Coordinate [mm]');
    ylabel('Static Pressure [Pa]');
    title('Static Pressure Distribution at Outlet, Corner Geomtry');

% POROUS_5mm (11) Initial Plot
figure;
    plot(y11_coord_mm_reodered, stat_press11, 'LineWidth', 1.5);
    grid on;
    ax = gca;
    ax.XAxis.Exponent = 0;
    ax.YAxis.Exponent = 0;
    xlim([0 1100]);
    ylim([60000 210000]);
    xlabel('Y-Coordinate [mm]');
    ylabel('Static Pressure [Pa]');
    title('Static Pressure Distribution at Outlet, Porous 5mm Geometry');

```

```
% POROUS_10mm (22) Initial Plot
figure;
    plot(y22_coord_mm_reodered, stat_press22, 'LineWidth', 1.5);
    grid on;
    ax = gca;
    ax.XAxis.Exponent = 0;
    ax.YAxis.Exponent = 0;
    xlim([0 1100]);
    ylim([60000 210000]);
    xlabel('Y-Coordinate [mm]');
    ylabel('Static Pressure [Pa]');
    title('Static Pressure Distribution at Outlet, Porous 10mm Geometry');

% POROUS_15mm (33) Initial Plot
figure;
    plot(y33_coord_mm_reodered, stat_press33, 'LineWidth', 1.5);
    grid on;
    ax = gca;
    ax.XAxis.Exponent = 0;
    ax.YAxis.Exponent = 0;
    xlim([0 1100]);
    ylim([60000 210000]);
    xlabel('Y-Coordinate [mm]');
    ylabel('Static Pressure [Pa]');
    title('Static Pressure Distribution at Outlet, Porous 15mm Geometry');

%% Pressure Ratio Calculations
clc;

% Pressure Ratios Immediatly Before and After Shockwave
% CORNER (0)
p1_0 = 74090.9; % Pa
y1_0 = 278.87; % mm
p2_0 = 201045; % Pa
y2_0 = 211.8; % mm
p2_p1_0 = p2_0 / p1_0; % Ratio

% POROUS_5mm (11)
p1_11 = 74361.9; % Pa
y1_11 = 264.655; % mm
p2_11 = 182871; % Pa
y2_11 = 216.16; % mm
p2_p1_11 = p2_11 / p1_11; % Ratio

% POROUS_10mm (22)
p1_22 = 74716.6; % Pa
y1_22 = 251.204; % mm
p2_22 = 176102; % Pa
y2_22 = 202.709; % mm
p2_p1_22 = p2_22 / p1_22; % Ratio

% POROUS_15mm (33)
p1_33 = 75310.8; % Pa
y1_33 = 234.507; % mm
```

```
p2_33 = 170159; % Pa
y2_33 = 188.681; % mm
p2_p1_33 = p2_33 / p1_33; % Ratio

fprintf('CORNER Pressure Ratio, p2/p1 = %.4f\n', p2_p1_0);
fprintf('POROUS_5mm Pressure Ratio, p2/p1 = %.4f\n', p2_p1_11);
fprintf('POROUS_10mm Pressure Ratio, p2/p1 = %.4f\n', p2_p1_22);
fprintf('POROUS_15mm Pressure Ratio, p2/p1 = %.4f\n\n', p2_p1_33);

%% Displacement Distance Calculations (shockwave height at Outlet)
% clc;

% CORNER (0)
d_star_0 = ((y1_0 - y2_0) / 2) + y2_0; % mm
% POROUS_5mm (11)
d_star_11 = ((y1_11 - y2_11) / 2) + y2_11; % mm
% POROUS_10mm (22)
d_star_22 = ((y1_22 - y2_22) / 2) + y2_22; % mm
% POROUS_15mm (33)
d_star_33 = ((y1_33 - y2_33) / 2) + y2_33; % mm

fprintf('CORNER Displacement Distance = %.4f mm\n', d_star_0);
fprintf('POROUS_5mm Displacement Distance = %.4f mm\n', d_star_11);
fprintf('POROUS_10mm Displacement Distance = %.4f mm\n', d_star_22);
fprintf('POROUS_15mm Displacement Distance = %.4f mm\n', d_star_33);

%% Creating Arrays of Combined Results

% Number of Bleed Holes for each geometry
BleedHoleDiams11 = [0, 5, 10, 15]; % mm

% Pressure Ratio for each geometry
p_ratios_array11 = [p2_p1_0, p2_p1_11, p2_p1_22, p2_p1_33];

% Displacement Distance for each geometry
disp_array11 = [d_star_0, d_star_11, d_star_22, d_star_33];

%% Individual Plots of Static Pressure Distribution for Each Geomety

% CORNER (0)
figure;
    plot(y0_coord_mm_reodered, stat_press0, 'LineWidth', 1.5);
    hold on;
    xline(y2_0, '--');
    xline(y1_0, '-');
    grid on;
    ax = gca;
    ax.XAxis.Exponent = 0;
    ax.YAxis.Exponent = 0;
    xlim([0 1100]);
    ylim([60000 210000]);
    xlabel('Y-coordinate [mm]')
    ylabel('Pressure [Pa]');
    title('Static Pressure Distribution at Outlet, Corner Geometry');
```

```
    legend('Outlet Pressure', 'p2 region Post-shock', 'p1 region Pre-shock');

% POROUS_5mm (11)
figure;
    plot(y11_coord_mm_reodered, stat_press11, 'LineWidth', 1.5);
    hold on;
    xline(y2_11, '--');
    xline(y1_11, '-');
    grid on;
    ax = gca;
    ax.XAxis.Exponent = 0;
    ax.YAxis.Exponent = 0;
    xlim([0 1100]);
    ylim([60000 210000]);
    xlabel('Y-coordinate [mm]')
    ylabel('Pressure [Pa]');
    title('Static Pressure Distribution at Outlet, Porous 5mm Geometry');
    legend('Outlet Pressure', 'p2 region Post-shock', 'p1 region Pre-shock');

% POROUS_10mm (22)
figure;
    plot(y22_coord_mm_reodered, stat_press22, 'LineWidth', 1.5);
    hold on;
    xline(y2_22, '--');
    xline(y1_22, '-');
    grid on;
    ax = gca;
    ax.XAxis.Exponent = 0;
    ax.YAxis.Exponent = 0;
    xlim([0 1100]);
    ylim([60000 210000]);
    xlabel('Y-coordinate [mm]')
    ylabel('Pressure [Pa]');
    title('Static Pressure Distribution at Outlet, Porous 10mm Geometry');
    legend('Outlet Pressure', 'p2 region Post-shock', 'p1 region Pre-shock');

% POROUS_15mm (33)
figure;
    plot(y33_coord_mm_reodered, stat_press33, 'LineWidth', 1.5);
    hold on;
    xline(y2_33, '--');
    xline(y1_33, '-');
    grid on;
    ax = gca;
    ax.XAxis.Exponent = 0;
    ax.YAxis.Exponent = 0;
    xlim([0 1100]);
    ylim([60000 210000]);
    xlabel('Y-coordinate [mm]')
    ylabel('Pressure [Pa]');
    title('Static Pressure Distribution at Outlet, Porous 15mm Geometry');
    legend('Outlet Pressure', 'p2 region Post-shock', 'p1 region Pre-shock');

%% COMBINED Plots of Results
```

```
266
267 fig_width_comb2 = 6;
268 fig_height_comb2 = 3.75;
269
270 % Combined RANGED View of Static Pressure Distribution for Each Geomety
271 figure('Name','Combined Pressues-BleedHoleDiam','Units','inches','Position',...
272     [1, 1, fig_width_comb2, fig_height_comb2]);
273     plot(y0_coord_mm_reodered, stat_press0, 'LineWidth', 2.5);
274     hold on;
275     plot(y11_coord_mm_reodered, stat_press11, 'LineWidth', 2);
276     hold on;
277     plot(y22_coord_mm_reodered, stat_press22, 'LineWidth', 1.5);
278     hold on;
279     plot(y33_coord_mm_reodered, stat_press33, 'LineWidth', 1.0);
280     grid on;
281     ax = gca;
282     ax.XAxis.Exponent = 0;
283     ax.YAxis.Exponent = 0;
284     xlim([0 1100]);
285     ylim([60000 210000]);
286     xlabel('Radial Distance at Outlet, y [mm]')
287     ylabel('Pressure [Pa]');
288     % title('Static Outlet Pressure Distribution with Variable Bleed Hole Diameter');
289     legend('No Porosity', '5mm Hole Diameter', '10mm Hole Diameter', '15mm Hole Diameter'
        );
290
291 %% Data Trends Plots of Results
292 fig_width_trends1 = 5.5;
293 fig_height_trends1 = 4;
294
295 % Pressure Ratio as a Function of Hole Diameter
296 figure('Name','PressureRatio_Vs_BleedHoleDiam','Units','inches','Position',...
297     [1, 1, fig_width_trends1, fig_height_trends1]);
298     plot(BleedHoleDiams11, p_ratios_array11, '-om', 'LineWidth', 1.5);
299     hold on;
300     % scatter(BleedHoleDiams11, p_ratios_array11, 'LineWidth', 2.5);
301     grid on;
302     xlabel('Bleed Hole Diameter, D [mm]')
303     ylabel('Pressure Ratio, p_2/p_1');
304     % title('Pressure Ratio as a function of Bleed Hole Diameter');
305     legend('Varying Hole Diameter Geometries');
306
307 % Displacement Distance as a Function of Hole Diameter
308 figure('Name','DispDistance_Vs_BleedHoleDiam','Units','inches','Position',...
309     [1, 1, fig_width_trends1, fig_height_trends1]);
310     plot(BleedHoleDiams11, disp_array11, '-ob', 'LineWidth', 1.5);
311     hold on;
312     % scatter(BleedHoleDiams11, disp_array11, 'LineWidth', 2.5);
313     grid on;
314     xlabel('Bleed Hole Diameter, D [mm]')
315     ylabel('Displacement Distance, \deltaˆ* [mm]');
316     % title('Displacement Distance as a function of Bleed Hole Diameter');
317     legend('Varying Hole Diameter Geometries');
318
```

```
%% Data Trends Plots of Results - Side-by-Side
fig_width_trends2 = 13;
fig_height_trends2 = 5;

figure('Name','Trends_Plots-BleedHoleDiam','Units','inches','Position',...
    [1, 1, fig_width_trends2, fig_height_trends2]);
    subplot(1, 2, 1)
        plot(BleedHoleDiams11, p_ratios_array11, 'LineWidth', 1.5);
        hold on;
        scatter(BleedHoleDiams11, p_ratios_array11, 'LineWidth', 2.5);
        grid on;
        xlabel('Bleed Hole Diameter [mm]')
        ylabel('Pressure Ratio, p_2/p_1');
        title('Pressure Ratio as a Function of Bleed Hole Diameter');
    subplot(1, 2, 2)
        plot(BleedHoleDiams11, disp_array11, 'LineWidth', 1.5);
        hold on;
        scatter(BleedHoleDiams11, disp_array11, 'LineWidth', 2.5);
        grid on;
        xlabel('Bleed Hole Diameter [mm]')
        ylabel('Displacement Distance, \delta^* [mm]');
        title('Displacement Distance as a Function of Bleed Hole Diameter');
```

Appendix E
MATLAB Script: Wall Data Analysis for Varying Hole Quantity Configurations

```
%% Analysis of Wall Data of Vh4-2 Geometry, Constant Hole Diameter Case
% By: Mathias Guillen

%% Import Data

clear; clc;

% CORNER (0) Geometry Data
stat_press_horz_wall_raw_0 = 'stat_press_horz_wall_data_Corner0';
data_0 = readmatrix(stat_press_horz_wall_raw_0, ...
                    'FileType', 'text', ...
                    'Delimiter', ',', ...
                    'NumHeaderLines', 1);
node_num0 = data_0(:,1);
x0_coord_m = data_0(:,2);
y0_coord_m = data_0(:,3);
stat_press0 = data_0(:,4);

% POROUS_4 (1) Geometry Data
stat_press_horz_wall_raw_1 = 'stat_press_horz_wall_data_Porous1';
data_1 = readmatrix(stat_press_horz_wall_raw_1, ...
                    'FileType', 'text', ...
                    'Delimiter', ',', ...
                    'NumHeaderLines', 1);
node_num1 = data_1(:,1);
x1_coord_m = data_1(:,2);
y1_coord_m = data_1(:,3);
stat_press1 = data_1(:,4);

% POROUS_8 (2) Geometry Data
stat_press_horz_wall_raw_2 = 'stat_press_horz_wall_data_Porous2';
data_2 = readmatrix(stat_press_horz_wall_raw_2, ...
                    'FileType', 'text', ...
                    'Delimiter', ',', ...
                    'NumHeaderLines', 1);
node_num2 = data_2(:,1);
x2_coord_m = data_2(:,2);
y2_coord_m = data_2(:,3);
stat_press2 = data_2(:,4);

% POROUS_12 (3) Geometry Data
stat_press_horz_wall_raw_3 = 'stat_press_horz_wall_data_Porous3';
data_3 = readmatrix(stat_press_horz_wall_raw_3, ...
                    'FileType', 'text', ...
                    'Delimiter', ',', ...
                    'NumHeaderLines', 1);
node_num3 = data_3(:,1);
x3_coord_m = data_3(:,2);
y3_coord_m = data_3(:,3);
```

```
stat_press3 = data_3(:,4);

% display(x0_coord_m)

%% Parsing and Adjusting Data
clc;

% Converting Coords from meters to millimeters
x0_coord_mm = x0_coord_m * 1000;
y0_coord_mm = y0_coord_m * 1000;

x1_coord_mm = x1_coord_m * 1000;
y1_coord_mm = y1_coord_m * 1000;

x2_coord_mm = x2_coord_m * 1000;
y2_coord_mm = y2_coord_m * 1000;

x3_coord_mm = x3_coord_m * 1000;
y3_coord_mm = y3_coord_m * 1000;

%% Max and Average Static Pressure Calculations for Each Geometry
clc;

maxPressure0 = max(stat_press0) * 0.001;
avgPressure0 = mean(stat_press0) * 0.001;
minPressure0 = min(stat_press0) * 0.001;

maxPressure1 = max(stat_press1) * 0.001;
avgPressure1 = mean(stat_press1) * 0.001;
minPressure1 = min(stat_press1) * 0.001;

maxPressure2 = max(stat_press2) * 0.001;
avgPressure2 = mean(stat_press2) * 0.001;
minPressure2 = min(stat_press2) * 0.001;

maxPressure3 = max(stat_press3) * 0.001;
avgPressure3 = mean(stat_press3) * 0.001;
minPressure3 = min(stat_press3) * 0.001;

fprintf('Max Stat. Press., Corner = %.4f kPa\n', maxPressure0);
fprintf('Max Stat. Press., Porous 4 = %.4f kPa\n', maxPressure1);
fprintf('Max Stat. Press., Porous 8 = %.4f kPa\n', maxPressure2);
fprintf('Max Stat. Press., Porous 12 = %.4f kPa\n\n', maxPressure3);

fprintf('Mean Stat. Press., Corner = %.4f kPa\n', avgPressure0);
fprintf('Mean Stat. Press., Porous 4 = %.4f kPa\n', avgPressure1);
fprintf('Mean Stat. Press., Porous 8 = %.4f kPa\n', avgPressure2);
fprintf('Mean Stat. Press., Porous 12 = %.4f kPa\n\n', avgPressure3);

fprintf('Min Stat. Press., Corner = %.4f kPa\n', minPressure0);
fprintf('Min Stat. Press., Porous 4 = %.4f kPa\n', minPressure1);
fprintf('Min Stat. Press., Porous 8 = %.4f kPa\n', minPressure2);
fprintf('Min Stat. Press., Porous 12 = %.4f kPa\n\n', minPressure3);
```

Appendix F
MATLAB Script: Wall Data Analysis for Varying Hole Diameter Configurations

```
%% Analysis of Wall Data of Vh4-2 Geometry, Constant Hole Number Case
% By: Mathias Guillen

%% Import Data

clear; clc;

% CORNER (0) Geometry Data
stat_press_horz_wall_raw_0 = 'stat_press_horz_wall_data_Corner0';
data_0 = readmatrix(stat_press_horz_wall_raw_0, ...
                    'FileType', 'text', ...
                    'Delimiter', ',', ...
                    'NumHeaderLines', 1);
node_num0 = data_0(:,1);
x0_coord_m = data_0(:,2);
y0_coord_m = data_0(:,3);
stat_press0 = data_0(:,4);

% POROUS_5mm (11) Geometry Data
stat_press_horz_wall_raw_11 = 'stat_press_horz_wall_data_Porous11';
data_11 = readmatrix(stat_press_horz_wall_raw_11, ...
                    'FileType', 'text', ...
                    'Delimiter', ',', ...
                    'NumHeaderLines', 1);
node_num11 = data_11(:,1);
x11_coord_m = data_11(:,2);
y11_coord_m = data_11(:,3);
stat_press11 = data_11(:,4);

% POROUS_10mm (22) Geometry Data
stat_press_horz_wall_raw_22 = 'stat_press_horz_wall_data_Porous22';
data_22 = readmatrix(stat_press_horz_wall_raw_22, ...
                    'FileType', 'text', ...
                    'Delimiter', ',', ...
                    'NumHeaderLines', 1);
node_num22 = data_22(:,1);
x22_coord_m = data_22(:,2);
y22_coord_m = data_22(:,3);
stat_press22 = data_22(:,4);

% POROUS_15mm (33) Geometry Data
stat_press_horz_wall_raw_33 = 'stat_press_horz_wall_data_Porous33';
data_33 = readmatrix(stat_press_horz_wall_raw_33, ...
                    'FileType', 'text', ...
                    'Delimiter', ',', ...
                    'NumHeaderLines', 1);
node_num33 = data_33(:,1);
x33_coord_m = data_33(:,2);
y33_coord_m = data_33(:,3);
```

```
stat_press33 = data_33(:,4);

% display(x0_coord_m)

%% Parsing and Adjusting Data
clc;

% Converting Coords from meters to millimeters
x0_coord_mm = x0_coord_m * 1000;
y0_coord_mm = y0_coord_m * 1000;

x11_coord_mm = x11_coord_m * 1000;
y11_coord_mm = y11_coord_m * 1000;

x22_coord_mm = x22_coord_m * 1000;
y22_coord_mm = y22_coord_m * 1000;

x33_coord_mm = x33_coord_m * 1000;
y33_coord_mm = y33_coord_m * 1000;

%% Max and Average Static Pressure Calculations for Each Geometry
clc;

maxPressure0 = max(stat_press0) * 0.001;
avgPressure0 = mean(stat_press0) * 0.001;
minPressure0 = min(stat_press0) * 0.001;

maxPressure11 = max(stat_press11) * 0.001;
avgPressure11 = mean(stat_press11) * 0.001;
minPressure11 = min(stat_press11) * 0.001;

maxPressure22 = max(stat_press22) * 0.001;
avgPressure22 = mean(stat_press22) * 0.001;
minPressure22 = min(stat_press22) * 0.001;

maxPressure33 = max(stat_press33) * 0.001;
avgPressure33 = mean(stat_press33) * 0.001;
minPressure33 = min(stat_press33) * 0.001;

fprintf('Max Stat. Press., Corner = %.4f kPa\n', maxPressure0);
fprintf('Max Stat. Press., Porous 5mm = %.4f kPa\n', maxPressure11);
fprintf('Max Stat. Press., Porous 10mm = %.4f kPa\n', maxPressure22);
fprintf('Max Stat. Press., Porous 15mm = %.4f kPa\n\n', maxPressure33);

fprintf('Mean Stat. Press., Corner = %.4f kPa\n', avgPressure0);
fprintf('Mean Stat. Press., Porous 5mm = %.4f kPa\n', avgPressure11);
fprintf('Mean Stat. Press., Porous 10mm = %.4f kPa\n', avgPressure22);
fprintf('Mean Stat. Press., Porous 15mm = %.4f kPa\n\n', avgPressure33);

fprintf('Min Stat. Press., Corner = %.4f kPa\n', minPressure0);
fprintf('Min Stat. Press., Porous 5mm = %.4f kPa\n', minPressure11);
fprintf('Min Stat. Press., Porous 10mm = %.4f kPa\n', minPressure22);
fprintf('Min Stat. Press., Porous 15mm = %.4f kPa\n\n', minPressure33);
```